This is to certify that the

thesis entitled

Phase-Stepped Digital Speckle Pattern Interferometry (DSPI) and Its Application to Mechanical Joining of Composite Materials

presented by

Francesco Lanza di Scalea

has been accepted towards fulfillment of the requirements for

Master's degree in Mechanics

Gary Lee Cloud
Major professor

Date 24 June 1996

PHASE-STEPPED DIGITAL SPECKLE PATTERN INTERFEROMETRY (DSPI) AND ITS APPLICATION TO MECHANICAL JOINING OF COMPOSITE MATERIALS

By

Francesco Lanza di Scalea

A THESIS

Submitted to
Michigan State University
in partial fulfillment of the requirements
for the degree of

MASTER OF SCIENCE

Department of Materials Science and Mechanics

1996

ABSTRACT

PHASE-STEPPED DIGITAL SPECKLE PATTERN INTERFEROMETRY (DSPI) AND ITS APPLICATION TO MECHANICAL JOINING OF COMPOSITE MATERIALS

By

Francesco Lanza di Scalea

In this work an in-plane sensitive setup of a Digital Speckle Pattern Interferometer (DSPI) together with a commercial four-bucket phase stepping algorithm is used for high-precision measurements. The displacement maps are fitted with least-square polynomials which are eventually differentiated along different directions to obtain strains. A comparison with results from electrical resistance strain gages in a cantilever beam experiment is used to verify the accuracy of DSPI for strain analysis.

The technique is then applied to the study of mechanically fastened composites. The strain/stress field around a single pin in a $[0°/90°]_S$ glass fiber-reinforced epoxy laminate loaded in tension through the pin is determined. The effect of an interference fit between the pin and the hole on the stress distribution is investigated for a static load. Results for a case of perfect fit and two cases of interference fit are compared. A substantial decrease, up to 50%, in stress concentration factor is observed when an interference fit is used.

ACKNOWLEDGMENTS

The author wishes to offer his sincerest appreciation and gratitude to his advisor and major professor Dr. Gary Lee Cloud for his continuous and valuable guidance during the course of this research.

He also wishes to thank Dr. Robert Soutas-Little for his encouragement and support throughout the author's course of study at Michigan State University.

The author extends his gratitude to Henry Wede and Xiaolu Chen for their helpful assistance and discussions.

TABLE OF CONTENTS

LIST OF TABLES

LIST OF FIGURES

CHAPTER I

INTRODUCTION

1.1 Problem outline and choice of experimental technique

Due to their high strength-to-weight ratio, composite materials have been used extensively in aircraft, space vehicles and ground transportation vehicles, as well as in sporting goods, medical equipment, prostheses and others. Like many other structural designs, members made of composite must also be joined together. Because of the anisotropic and heterogeneous nature, the joint problem in composites is more difficult to analyze than is the case with isotropic materials. Two methods frequently used are bonded joints and mechanically fastened joints. The former is preferred for the joining of major structural members. On the other hand, the latter approach is less expensive but less widely used. One of the possible reasons is the lack of a comprehensive understanding of the detailed stress distribution in such mechanically fastened joints. For anisotropic materials the stress distribution is strongly dependent upon several parameters such as material properties, laminate lay-up, ply orientation, friction, clearance and interference between mechanical fastener and hole, etc. A further understanding of the stress distribution around pin-loaded holes in composites would be very useful for estimating the strength of such a joint.

Interference fit pins are used to lower the stress concentration factors and to reduce the magnitude of the local oscillatory stress component in the case of oscillatory loads and thereby increase the fatigue life of the component. Not many studies have been done on the effects of interference on composite materials and, as mentioned earlier, several parameters contribute to complicate the stress field around the hole in this case.

Most of the studies done on this application in the past have been numerical and theoretical. More experimental results are needed in order to gain a better understanding of this complex problem. A full-field analysis of the deformation field on the surface of the object seems to be the most suitable approach.

Transmission photoelasticity has been used successfully to study stress-concentrations around holes in isotropic material plates (Jessop, Snell and Holister 1956 and 1958, Lambert and Brailey 1962, Frocht and Hill 1940), but it cannot be used for opaque composite materials.

Strain gages have been used to study the same problem (Frocht and Hill 1940, Regalbuto and Wheeler 1970), but they have the obvious disadvantage of being a pointwise technique and not being able to represent accurately high strain spatial gradients such as those around a loaded hole.

Speckle photography has been used for interference fit fastener investigations (Ford *et al.* 1975), but the main disadvantages are that this technique requires photographic films and gives rise to a loss of definition resulting from speckle effects in the fringe photograph. Furthermore this technique has sensitivity limits determined by film resolution and camera aperture (Cloud 1995).

Moire interferometry has been used successfully to study stress concentrations around loaded and non-loaded holes in composite tensile members (Herrera Franco 1985, Cloud *et al.* 1987, Czarnek, Post and Guo 1987), but this method requires the replication of a diffraction grating on the specimen and the use of photographic plates.

In the present work, phase-stepped Digital Speckle Pattern Interferometry (DSPI) has been used. Since, in the case of a pin-loaded hole in a tension plate, the displacements are predominantly parallel to the surface of the object, the in-plane sensitive arrangement of DSPI has been employed. DSPI is a variation of Electronic Speckle Pattern Interferometry (ESPI) which processes speckle data inside a computer rather than in an analog device (Creath 1984). It is an accurate, non-invasive, quick and simple technique for full-field stress analysis. No photographic processing is involved, and the method doesn't require particularly stable environments. This makes DSPI a potential substitute for Moire interferometry and strain gages.

Phase-stepped DSPI has been used in the recent years for measurement of both the out-of-plane and the in-plane components of the displacement of the surface of an object for static loading (mechanical or thermal) and dynamic loading. This method has also been used for contouring of complicated structures. Only a few studies with this technique have been conducted for strain/stress analysis.

1.2 Objective and scope

The main objectives in this research are:

a) To verify that phase-stepped Digital Speckle Pattern Interferometry is a quick and accurate method for full-field strain/stress analysis.

b) To study the strain/stress field around a single pin in fiber-reinforced plastic laminate loaded in tension through the pin.

c) To study the reduction in stress concentration factors resulting from the introduction of an interference fit between pin and hole in composite materials.

1.3 Relevant literature

1.3.1 Application of Speckle Interferometry to metrology

Digital Speckle Pattern Interferometry (DSPI) is a well-established tool in the mapping of vibration, displacement or deformation fields. A review paper covers some of the latest developments in DSPI (Joenathan 1991).

In dynamic analysis, time-averaged, pulsed laser, phase modulation and stroboscopic methods have been employed. In-plane vibration of objects has been studied by Mendoza Santoyo, Shellabear and Tyrer (1991) using DSPI. In the in-plane sensitive setup of DSPI, they used a pulsed laser, which illuminated the object at different points in the vibration cycle, and the single phase step technique, which only requires two fringe patterns at 0° and 90° phase difference between the beams, to obtain quantitative information about the amplitude, direction and phase of vibration over the field.

Joenathan and Khorana (1992) investigated the effect of speckle averaging in a study of the out-of-plane vibration modes of a plate. They used a fiber-optic out-of-plane-sensitive DSPI setup with π and $\pi/2$ phase-stepping methods. They found an optimum number of acquired frames to be superimposed for a certain state of the object, which gives maximum contrast of the resultant correlation fringes.

DSPI has also been used for generating contours of diffuse objects. This technique overcomes some of the drawbacks suffered by the already existing optical methods, such as holographic methods. The advantage of DSPI is that intermediate photographic processing is eliminated. Joenathan, Pfister and Tiziani (1990) studied contouring of an object by employing a dual beam illumination DSPI technique. They analyzed the sensitivity and the orientation of the contour planes. Two exposures were made with the object tilted between the exposures, and the subtracted speckle pattern consisted of fringes representative of the shape depth of the test surface. To obtain quantitative data about the shape of the surface of the object, they used a three-step phase-shifting technique.

Instead of tilting the test object, a new method for DSPI contouring has recently been reported. It involves shifting the illumination beams in the case of either one illumination beam with one reference beam (Winther and Slettemoen 1984) or dual-beam illumination (Zou *et al.* 1992). The two images before and after shifting are subtracted from one another to obtain interference contour fringes across the object, similar to the projected fringes of projection Moire.

Zou *et al.* (1992) proposed an arrangement for contouring by DSPI with four illumination beams, thereby making it unnecessary to move anything during measurements.

Since DSPI is non-contacting, fast and sensitive, it has also been used for non-destructive inspections. Cloud and Nokes (1993) conducted investigations to detect internal defects in graphite epoxy materials and examined the relative sensitivity of DSPI and another interferometric technique, Electronic Shereography (ES). Both thermal and mechanical loading were used. Damages caused anomalies in the correlation fringe patterns and therefore could be detected.

Ratnam, Evans and Tyrer (1992) used DSPI to measure the radial expansion of a heated diesel engine piston. A simple "mirror" concept enabled simultaneous measurement of in-plane and out-of-plane components of displacements. A three-stage phase-stepping technique was used to measure the displacements. Before being processed, the images were low-pass filtered to remove the high-frequency noise.

Gulker *et al.* (1990) used DSPI for *in situ* deformation monitoring on buildings. They determined the out-of-plane component of the displacement by evaluating the correlation fringes generated in a transportable speckle interferometer. To determine the direction of the displacements in the object, they used continuous fringe observation.

Preater (1984) used pulsed laser DSPI to measure in-plane displacement on rotating components. He was able to record interference subtraction fringes for component tangential velocities up to $15 ms^{-1}$.

DSPI coupled with the phase-shifting technique can give quantitative detailed information on the displacement fields in an object surface. When the strain/stress fields are to be determined, a further step must be taken: the displacement maps must be differentiated along different directions. Vrooman and Maas (1991) used phase-stepped Speckle Interferometry to determine surface strains in a T-shaped aluminum test object. They first determined the three components of the displacement vector at each object point by performing three measurements with different sensitivity vectors and using a four-step phase shifting technique. They then calculated the three components of the surface strain (the two normal strains and the shear strain) by differentiating the displacement maps along the two in-plane axes. The upper limit of the measuring range of the strain in their setup was ~200μstrain for a 100×100 mm^2 object region. The application of a smoothing filter to reduce phase errors caused by speckle decorrelation, gave a repeatability of the measured strains at each pixel of ~0.3 μstrain rms.

Jia and Shah (1994) used in-plane DSPI to observe the displacement and strain fields in the fracture of carbon-fiber-reinforced concrete specimens subjected to tension. Their setup was a two-dimensional in-plane displacement-sensitive interferometer consisting of two single DSPI systems, each to measure independently one of the the two in-plane components of the displacement. Qualitative information about fracture processes, crack initiation and crack propagation were extracted by monitoring the correlation fringes continuously and in real time. The quantitative analysis was carried out through an analysis of the sensitivity vector for two-dimensional DSPI. After determining the displacements, the strains were calculated using a least-square surface-fitting method. The discrete two components of displacement were fitted with two plane surface functions which were eventually differentiated along two in-plane directions to obtain normal and shear strains.

DSPI has been used by Vikhagen and Malmo (1991) to measure deformations in polymer laminates and concrete. They used a max-min scanning phase-shifting procedure to measure the deformation. Before calculating the spatial gradients of the deformation, the phase images were smoothed to reduce the noise level. They were able to detect cracks with length less than 1mm in a concrete specimen in a pressure test, using the fact that cracks spatially shift the deformation gradient (strain) displayed on the video monitor and therefore are easily detected. The crack propagation could be also monitored.

1.3.2 Study of pin-loaded holes in mechanical structures

Several studies on mechanical joints and specifically pin-loaded holes have been conducted in the past, and some of them are mentioned here.

A review paper on the strength of mechanically fastened joints in fiber-reinforced plastics was written by Godwin and Matthews (1980). Effects of material parameters, fastener parameters and design parameters are summarized and discussed.

Chang, Scott and Springer (1984) presented methods for sizing composite laminates containing one or several pin loaded holes in order to obtain maximum failure load .

The stress field around pin-loaded holes in composite plates has been studied *numerically* in the past. Pradhan and Ray (1984) did a finite element investigation of the stress distribution around pin-loaded holes and gave results for isotropic as well as fiber reinforced plastic composite materials. They considered the case of full contact (contact angle=180°) and that of partial contact (contact angle<180°) between pin and hole. They found that the maximum circumferential stress at the edge of the hole depends strongly on the material properties as well as the ratio of hole diameter to width of the plate. This maximum stress was found to be high in the case of graphite/epoxy and boron/epoxy unidirectional laminae, with respect to glass/epoxy. Furthermore, this maximum circumferential stress was shown to depend strongly upon the contact angle between pin and hole. They also concluded that the rate of decay of stresses along the axis through the pin, perpendicular to the loading force, is higher in orthotropic plates then in isotropic plates, and the reverse is true for the stresses along the axis parallel to the loading force.

Matthews, Wong and Chryssafitis (1982) applied a three-dimensional finite element analysis and showed that the stress distribution around a loaded hole in fiber-reinforced laminates depends on whether the load is applied via a pin or a bolt. Values of stress concentration factors (SCF) for different geometries of the specimen are given and they are compared to results from other references.

Eriksson (1986) used finite element analysis to calculate contact stresses and stresses in the vicinity of the hole boundary, taking account of the contact problem. He studied effects of laminate elastic properties, clearance, friction and load magnitude and concluded that these parameters affect the stress distribution significantly.

Wong and Matthews (1981) conducted a two-dimensional finite element analysis of bolted joints in fiber reinforced plastic. They also compared the strain pattern in a two-hole joint with that in a single-hole joint.

Cohen *et al.* (1995) used finite element analysis to predict the strength of multifastener, thick composite joints. The stress fields around the fastener-loaded hole in both single and multifastener joints were determined. They then used the maximum strain criterion to locate possible sites of failure initiation and utilized this information in conjunction with the average stress criterion to predict the strength of the joint.

Some studies have also been done using *analytical* methods. Theocaris (1956) gave an analytical exact solution for the stress distribution resulting from loading a hole with a pin in isotropic materials. He examined different values of diameter of the hole.

Zhang and Ueng (1984) found an analytical solution of stresses around a pin-loaded hole in orthotropic plates using the complex stress functions which satisfy the displacement boundary conditions along the hole. They observed that the stress field is strongly affected by the elastic properties of the material and the presence of friction, which increases steadily the shear stress along the edge of the hole and concluded that decreasing the friction between pin and hole and keeping the pin load along the principal axis of higher Young's modulus will increase the ability to support the pin-load.

De Jong (1977) studied analytically the stress field near the hole in orthotropic and isotropic plates using Lekhnitskii's method of complex functions. He considered the hole loaded without friction on only a part of its edge. He showed that the stresses depend on the material properties.

The effect of pin elasticity, clearance and friction on the stresses in a pin-loaded orthotropic plate has been studied by Hyer, Klang and Cooper (1987) with the complex variable approach. They found that friction changes the sign of the circumferential stress in the bearing region and reduces the bearing stress. It also increases the peak circumferential stress. They also found that the contact angles change as the load level increases.

Collings (1977 and 1982) studied the strength of composite laminate joints for the different failure modes. He suggested that the inclusion of ±45° plies strengthens the laminate.

There have also been *experimental* studies of the pin-loaded hole problem. Cloud *et al.* (1987) studied experimentally the pin-loaded hole problem in orthotropic composites using high-sensitivity interferometric Moire and numerically with boundary element techniques. They examined multi-fastener arrays, load-spreading washers, bolt preload effects and field measurements.

Herrera Franco (1985) determined strain fields around a pin-loaded hole in isotropic and orthotropic specimens using high-sensitivity interferometric Moire. He observed a substantial reduction in stress concentration factors when an isotropic material insert is used between the hole and the pin.

Frocht and Hill (1940) used strain gages and photoelasticity to determine the stress concentration factors in isotropic plates loaded through pin in the hole. They studied also the effect of geometrical parameters of the joint.

Nisida and Saito (1966) used an interferometric method to study the stress distribution around a pin-loaded hole in isotropic materials.

1.3.3 Study of the effect of an interference fit

The effect of an interference-fitted pin on the stress distribution has been studied for both isotropic and orthotropic materials. Nevertheless, a complete understanding of the behaviour of such joints, especially in the case of anisotropic materials, is yet to be attained. It is hoped that this paper is a further step in the right direction.

Jessop *et al.* studied photoelastically the stress field near the hole for the cases of (1) load applied to the plate only (1956) , load applied (2) to pin only and (3) to pin and plate simultaneously (1958). Their studies were on isotropic materials and showed a reduction in stress concentration factors (SCF's) resulting from the introduction of an interference-fit pin in the hole. This effect was shown to be qualitatively the same for the case of load applied to the plate only and load applied to the pin. They also found that the decrease of SCF's depends on the ratio of interference stress to applied tension. When varying loads are applied to the pin or the plate, the effect of interference is to produce a rise in the mean stress level at critical points on the hole boundary with a marked fall in the oscillatory stress. This phenomenon leads to an increase of the fatigue life of the joint. There appears to be an optimum value of interference for given applied load at which the endurance of the joint will have its highest value.

Lambert and Brailey (1962) studied photoelastically the influence of the coefficient of friction on the stresses in a pin-joined connection with interference for isotropic materials. They found non-linearities in load transfer mechanism from the pin to the plate in the case of an interference fit (non-linear relation between applied load and maximum stresses in the plate), except at very high initial interference. They showed further that this behavior is due to relative slip between the two surfaces and therefore depends upon both the initial interference and the coefficient of friction between pin and hole. They concluded that, in order to fully obtain the benefits of the use of high interference fits in reducing the increment in stresses and enhancing the fatigue life of a joint under pulsating load, a high coefficient of friction between pin and hole coupled with a high initial interference fit is needed.

Frocht and Hill (1940) used strain gages and photoelasticity on isotropic material to obtain stress concentrations around the pin-loaded hole. They investigated the effect of geometry and clearance between pin and hole. In the case of clearance, they found variations in SCF's with the load.

Stress distributions from interference fits and uniaxial tension in isotropic plates were determined theoretically and experimentally using strain gages by Regalbuto and Wheeler (1970). They observed that interference prestress and load-induced stress cannot be simply added to calculate the resultant stress field, but they should be nonlinearly superimposed. The result is that application of a tensile load to the prestressed assembly decreases the change in stress level due to the applied load with respect to the case of no prestress: this smaller excursion contributes to increase the fatigue life of the member in the case of a varying pulsating load.

Numerical studies on interference fit pins in composite plates subjected to both pull and push type of loads have been performed by Ramamurthy (1989). He showed that interference increases fatigue life. Using finite element analysis, he found that the inteference fit pin exhibits partial contact/separation under the loads and the contact region is a non-linear function of the load magnitude. The same author, in another paper (1990), studied interference fit pin joints subjected to bearing bypass loads, finding similar non-linearities.

Sendeckyj and Richardson (1974) studied the fatigue behaviour of graphite/epoxy joints loaded through an interference fit pin and showed that increasing the level of interference increases the fatigue life.

Ford *et al.* (1975) gave a prescription for fatigue-life analysis and prediction for isotropic joints assembled with interference fit fasteners, using analytical and experimental techniques (speckle photography, strain gages and dislocation etching). They were able to determine stress fields due to interference along different directions in the specimen and observed the decrease in cyclic strain amplitude in fatigue tests when the degree of interference was increased, for three values of interference. They used loads that were large enough to induce plastic deformations around the hole.

In a survey paper on fasteners for composite structures, Cole, Bateh and Potter (1982) noted that interference fit pins are desirable not only to increase fatigue life but also to increase load-sharing in joints with multiple rows of fasteners and to retard fuel leakage in tank areas. They also pointed out that it is the low interlaminar strength of composites that restricts the use of interference fit for these materials.

CHAPTER II

DIGITAL SPECKLE PATTERN INTERFEROMETRY (DSPI)

2.1 Introduction

A comprehensive presentation of the main issues concerning Speckle Interferometry techniques has been given by Cloud (1995). His book has been the main source of information for this chapter.

2.2 The speckle effect

When an object with rough surface (on the scale of an optical wavelength, ~0.6 μm) is illuminated with a coherent light such as laser light, its visual or photographic image appears covered with a grainy structure as shown in Figure 1: this is what is known as "the speckle effect".

The origin of this effect is explained in Figure 2. When laser light is reflected or scattered from the "rough" surface of the object, the optical wave at any receiving point results from a combination of different waves coming from different points of the illuminated surface. The optical path lengths of these waves, from source to object point to receiving point, differ in general depending on surface roughness and the geometry of the system. These coherent waves interfere at the receiving point, giving rise at an irradiance that can be anything from dark to fully bright.

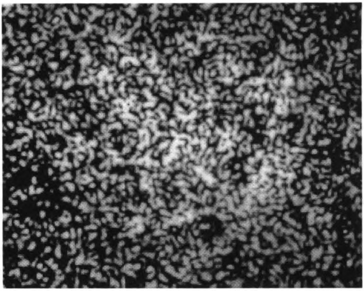

Figure 1. *A laser speckle pattern (from Cloud 1995).*

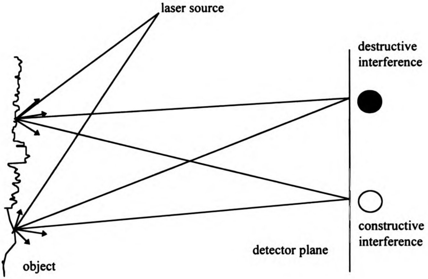

Figure 2. *The formation of a laser speckle pattern.*

In Figure 2 the two extreme cases of irradiance equal to zero ("destructive" interference $\rightarrow$ dark speckle) and maximum irradiance ("constructive" interference $\rightarrow$ bright speckle) are shown. This type is called "objective speckle", as opposed to "subjective speckle" which involves the presence of a lens to create an image of the object, in which case the diffraction limit of the lens must be considered. As a result of this, the waves creating an image do not travel from object point to image point. Rather they go from object "cell" to image "cell". The results are substantially the same as the case of "objective" speckle . As an example, any speckle observed by the eye involves the imaging optics of the eye and therefore is "subjective" speckle.

The speckle, regardless of whether is subjective or objective, has a known brightness probability density function that shows that the most probable brightness for a speckle is zero, i.e. there are more dark speckles in the field than bright speckles.

2.3 Speckle size

For subjective speckle the size S of the individual speckles is related to the aperture ratio F=focal length/diameter of aperture=f/a of the imaging lens (the f/No.), the magnification M of the lens and the wave length of the light λ.

The speckle size in the image is:

$$S \cong 1.22(1+M)\lambda F \tag{1}$$

From simple lens theory, the speckle size on the object is given by

$$S_{obj} \cong 1.22(1+M)\lambda \frac{F}{M} \tag{2}$$

This is defined as the resolution element on the object. The speckle size usually ranges between 5 and 50 μm.

Sometimes two speckle patterns are superimposed, such as with the in-plane sensitive setup. In this case the spatial frequency distribution of the combination of the two beams will be similar to that of either one of the two beams.

The minimum speckle size in this case is given by:

$$S_{min} \cong 1.22(1+M)\lambda F \tag{3}$$

The resolution limit of the detector array must be higher than S_{min} in order to resolve the speckle pattern.

2.4 Speckle Correlation Interferometry

Speckle Correlation Interferometry is a technique that uses the phase information within a speckle and the coherent combination of speckle fields as the basis of measurement. The phase data of the waves coming from different object points and interfering coherently to create a speckle are already converted to amplitude information. In this case, only the individual speckle irradiance can be recorded. In order to somehow record the phase data, specifically the average phase within one speckle cell, the speckle field must be combined with a reference beam (or just another speckle beam). In this way the phase changes between two images of the object corresponding to two different states of the object (undeformed and deformed state or two different deformed states) can be seen as correlation fringes which are representative of object displacement components.

Figure 3 is useful to understand what happens when a speckle field is combined with a reference field.

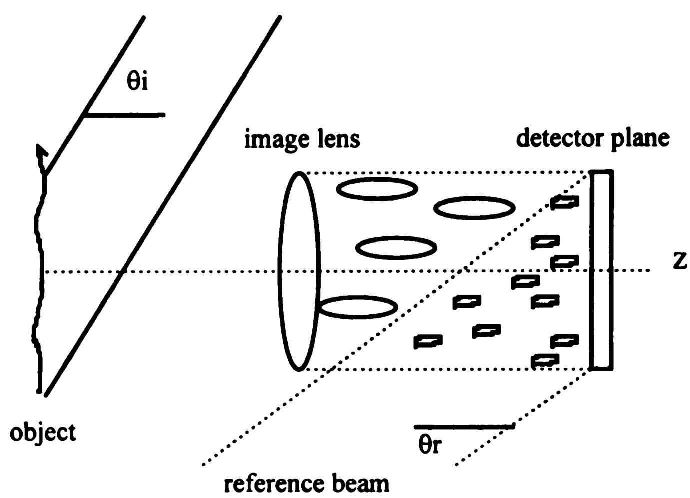

Figure 3. *Combination of a speckle field with a reference field in speckle correlation interferometry.*

The effect of the reference beam is to make the speckles very dependent on the phase difference between reference and object beams. The short speckle-producing waves give the idea that the average optical phase within a speckle becomes sensitive to z-axis displacements of the object when a reference beam with a nearly zero incidence angle is used. Sensitivity to out-of-plane motions is equal to that of holographic interferometry. The three modes of fringe observation of real-time, time-average and double-exposure are conceptually the same for the two techniques.

Speckle metrology involves recording and/or combining two speckle patterns for two states of the specimen. In order for Speckle Correlation Interferometry to function, the two speckle patterns have to be "correlated" with one another. "Correlated" means that these two fields have to be superimposed. There are two causes of loss of correlation in speckle metrology: phase decorrelation and memory loss.

Phase decorrelation: a speckle can be seen as a signature of a microscopic object surface element. If the displacements of the object are relatively large, an alteration of relative phase relationships within each speckle during speckle movement occurs, altering the fundamental speckle signature. It seems that a phase change of 2π from edge to edge across a given speckle results in total phase decorrelation (Cloud 1995).

Memory loss: when the object deforms, the resolution element also moves. If the movement is large enough so that each displaced speckle does not appreciably overlap the corresponding original speckle position, the displaced speckle cannot be compared with its first version. The maximum allowable motion of each speckle in speckle correlation interferometry is some fraction of the speckle diameter. If electronic detectors (photographic devices, sensing element in a CCD video device, etc.) are used, the movement of each speckle cannot be so large that the speckle is shifted across the detector element, in which case the detector would "lose memory" of the speckle which contains the displacement information. An implication of this is that speckle size should be large for speckle correlation interferometry.

Speckle decorrelation puts a limit on the range of measurements with speckle correlation interferometry.

Is should be mentioned that there is another technique based on the speckle effect called "Speckle Photography", where the speckles before and after the deformation must form a pair that is separated by a small distance in order to form a sort of grating. This method is complementary to Speckle Correlation Interferometry in terms of range and sensitivity of measurements.

Two arrangements of Speckle Correlation Interferomery have been developed in the past to measure in-plane and out-of-plane components of displacement.

2.4.1 Out-of-plane sensitive setup

A setup sensitive to the out-of-plane component of displacement is shown in Figure 4 (Jones and Wykes 1983). This setup has been used for several applications in speckle interferometry.

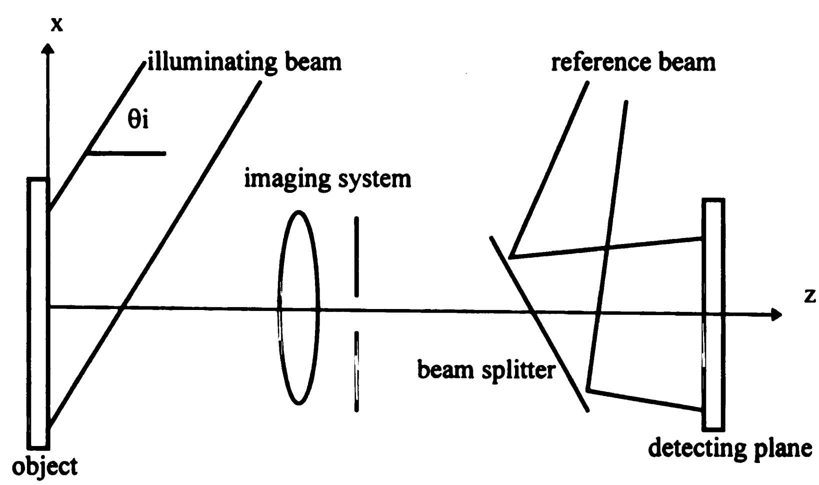

Figure 4. *Speckle interferometer sensitive to out-of-plane component of displacement.*

The z-axis is chosen to be the optical axis. The object is illuminated at an incidence angle θ_i (angle between illumination direction and normal to the object surface). A reference wave, which has usually either spherical or planar wave front and nominally normal incidence, is added to the image using a beam splitter. Applying the theory of the sensitivity vector (Vest 1979) with a viewing angle θ_v=0, the expression of the change $\Delta\phi$ in the phase of the object beam relative to the reference beam, point by point on the detecting plane is :

$$\Delta\phi = \left(\frac{2\pi}{\lambda}\right)\left(1+\cos\theta_i\right)d_z \tag{4}$$

where θ_i is the incidence angle of the illuminating beam, λ the wave length of the light used to illuminate the object and d_z the out-of-plane component of the displacement.

It should be noticed that for ordinary applications the incidence angle of the illuminating beam is considered constant across the illuminated object even if the beam has a spherical wave front (spherical wave front is easier to achieve because it doesn't require a collimating lens and also it's not easy and economical to obtain a large collimated beam to cover a large area). In the same fashion, a spherical wave front reference beam can be considered incident at a constant angle across the detecting plane. This approximation is more acceptable the further the object is from the expanding lens of the illuminating beam and the further the detecting plane is from the expanding lens of the reference beam. A quantitative analysis of the measurement errors induced by a variable sensitivity vector across the field has been done by Chen (1995). The case of cylindrical wave fronts in a dual-beam illumination DSPI setup is examined in Appendix A.

Assume that the system is operating in real-time mode. The brightness of the image, which is the negative of the original speckle pattern, varies as the specimen moves in the z-direction. A dark fringe in the image will occur in those points where $\Delta\phi$ =2nπ, n being an integer, i.e. wherever

$$dz = \frac{n\lambda}{\left(1+\cos\theta_i\right)} \tag{5}$$

n is the fringe order.

This means that the sensitivity of this method is

$$\frac{d_z}{n} = \frac{\lambda}{\left(1+\cos\theta_i\right)} \tag{6}$$

As a practical example, for λ=0.633 μm (He-Ne laser light) and θ_i=10° , it is

$$\frac{d_z}{n} = 0.32\mu m \tag{7}$$

This means that there is a fringe every 0.32 μm of displacement, which is a very high sensitivity. The maximum measurable displacement is limited by decorrelation and/or memory loss as explained earlier.

2.4.2 In-plane sensitive setup

In order to measure the in-plane component of the displacement, a dual-beam illumination setup is needed (Leendertz 1970). In this arrangement two object speckle patterns are combined coherently.

Referring to Figure 5, the object lies in the xy-plane, and the z-axis, normal to the object surface, is the viewing axis. The object is illuminated by two plane wave fronts inclined at equal and opposite angles θ with respect to the surface normal. Let $I_1(x,y)$ and $I_2(x,y)$ be respectively the light irradiances of the first and of the second object beam at the imaging plane. At any image point P, the irradiance resulting from the combination of the two beams is:

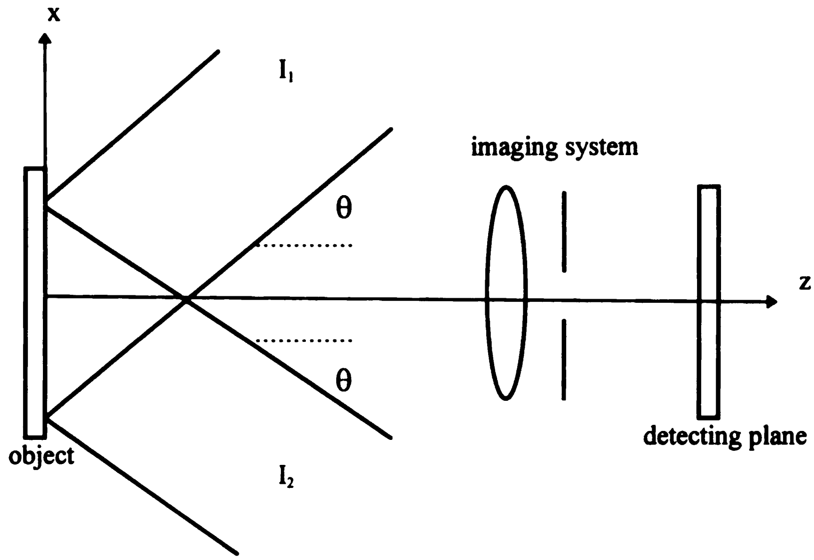

Figure 5. *Speckle interferometer sensitive to in-plane component of displacement.*

$$I = I_1 + I_2 + 2\sqrt{I_1 I_2}\cos\phi \qquad (8)$$

where ϕ is the phase difference between the two waves contributing to point P in the image at its initial state (1).

This is the typical interference equation, stating that the intensity in each point of an interferogram is a cosine function of the phase difference between the two light contributions arriving at the considered position.

If the object is displaced by a displacement vector **d** having generally three components d_x, d_y and d_z, the irradiance at P becomes:

(1) *The irradiance I of a beam is the time average of the square of the wave amplitude A of the beam. It represents the time average of the power density of the light.*

$$I = I_1 + I_2 + 2\sqrt{I_1 I_2}\cos(\phi - \Delta\phi) \tag{9}$$

where $\Delta\phi$ is the added phase difference induced by the displacement.

Using again the sensitivity vector theory, the total phase change in beam 1 is:

$$\delta_1 = (\mathbf{k}_3 - \mathbf{k}_1) \bullet \mathbf{d}$$

$$= \frac{2\pi}{\lambda}[\mathbf{k} - (-\sin\theta \cdot \mathbf{i} - \cos\theta \cdot \mathbf{k})] \cdot (d_x \cdot \mathbf{i} + d_y \cdot \mathbf{j} + d_z \cdot \mathbf{k})$$

$$= \frac{2\pi}{\lambda}[d_x \sin\theta + d_z(1 + \cos\theta)] \tag{10}$$

The total phase change in beam 2 is:

$$\delta_2 = (\mathbf{k}_3 - \mathbf{k}_2) \bullet \mathbf{d}$$

$$= \frac{2\pi}{\lambda}[\mathbf{k} - (\sin\theta \cdot \mathbf{i} - \cos\theta \cdot \mathbf{k})] \cdot (d_x \cdot \mathbf{i} + d_y \cdot \mathbf{j} + d_z \cdot \mathbf{k})$$

$$= \frac{2\pi}{\lambda}[-d_x \sin\theta + d_z(1 + \cos\theta)] \tag{11}$$

In equations (10) and (11): $\mathbf{k}_1$ and $\mathbf{k}_2$ are the unit vectors along the two illuminating directions, $\mathbf{k}_3$ is the unit vector along the viewing direction; **i**, **j** and **k** are the unit vectors along the (x,y,z) reference system.

The $\Delta\phi$ in equation (9) is the difference of δ_1 and δ_2, i.e.

$$\Delta\phi = \left(\frac{4\pi}{\lambda}\right) d_x \sin\theta \tag{12}$$

where θ is the illumination angle (angle between the direction of the illuminating beam and the normal to the object surface) and λ is the wave length of the light used.

A dark fringe in the image will occur in those points where $\Delta\phi = 2n\pi$, n being an integer, i.e. wherever

$$d_x = \frac{n\lambda}{2\sin\theta} \tag{13}$$

The parameter n in Equation (13) represents the fringe order.

The sensitivity of this setup is:

$$\frac{d_x}{n} = \frac{\lambda}{2\sin\theta} \tag{14}$$

As a practical example, for λ=0.633 μm (He-Ne laser light) and θ=30° , it is

$$\frac{d_x}{n} = 0.633\mu m \tag{15}$$

This means that there is a fringe every 0.633 μm of displacement. The maximum measurable displacement is again limited by decorrelation and/or memory loss.

For a complete analysis of the deformation of an object, the two in-plane components of the displacement need to be determined, in addition to the out-of-plane component. To measure the second in-plane component, either the optical setup or else the specimen must be rotated by 90° about the z-axis. Another solution is the use of a two-dimensional interferometer (Jia and Shah 1994) where the two components of the in-plane displacement are measured basically at the same time, avoiding errors due to imperfect repositioning of the elements after rotation by 90°.

The recent introduction of optical fiber technology in speckle interferometers (e.g. Joenathan and Khorana 1992) gives the system more flexibility and makes it easier to rotate the optical paths to measure both components of the displacement.

2.4.3 Recording speckle in speckle correlation interferometry

As an image recording device, a CCD (charge-coupled device) camera is usually used in speckle correlation interferometry. The camera is used in combination with an imaging lens.

The aperture of the imaging lens should be such that it matches the resolution of the camera, i.e. gives speckles which can be resolved by the camera detector array, which is typically a 512×512 pixel array. Increasing the aperture decreases the speckle size and therefore the correlation fringes are less grainy and smoother. Moreover, the required laser power can be reduced. Also, since more light illuminates the object, the speckle contrast and the speckle modulation increase. On the other hand, when the light levels are good, closing the aperture has the advantage of increasing the speckle size and thus increasing both contrast and modulation *on the detector array* (see Section 2.6.7). A larger speckle size means also an increase in range of measurements in correlation speckle interferometry. In adjusting the aperture there is therefore always a trade off . As a general rule of the thumb, the aperture of the viewing system should be set to the smallest diameter possible, consistent with a reasonable bright object beam.

The techniques to record the specklegram are the same as those used in holographic interferometry, i.e. real-time, time-average or double-time modes.

The system is sensitive to vibrations, when vibration amplitudes are larger than speckle size. Vibration isolated tables are usually used.

Specklegrams for correlation interferometry can be recorded in high-contrast photoplates. The resolution needed in the emulsion is not as high as the one required in holographic interferometry, especially if the system is designed to have large speckles. The possibility of recording specklegrams with electronic means avoids the use of photographic materials. This subject is discussed in Section 2.5.

2.4.4 Correlation fringe visibility

Fringe contrast in speckle correlation interferometry is low as compared to other types of interferometry. The highest contrast is achieved in real-time fringes, and the theoretical maximum visibility is on the order of 14%. Double exposure and time-average processes give very low contrast fringes, and the reason is that two speckle patterns have been incoherently added before film development. Areas where the two speckle patterns are correlated will have high-contrast speckles, whereas areas where the speckle patterns are uncorrelated will exhibit poorly contrasted speckles. Optical spatial filtering can improve fringe contrast.

With the advent of electronic image acquisition and computer fringe processing, contrast enhancement and digital filtering are used to substantially improve the visibility of correlation fringes. These new techniques are known as Digital Speckle Pattern Interferometry.

2.5 Digital Speckle Pattern Interferometry (DSPI)

2.5.1 Introduction

The basic idea of DSPI was developed in England by Butters and Leendertz (1971) and in the United States by Macovsky, Ramsey and Schaefer (1971). The use of television image acquisition and computer image processing has revolutionized optical methods of metrology. DSPI is a variation of Electronic Speckle Pattern Interferometry (ESPI), which processes speckle data inside a computer rather than in an analog device (Creath 1984). It measures components of displacement of an object surface. DSPI is also known as video holography or TV holography.

DSPI is an electronic version of Holographic Interferometry which uses a CCD camera instead of a photographic film to record the images. The resolution of the recording medium need not be high compared to that required for holography. This is due to the fact that only the speckle pattern must be resolved, the speckles being now the carriers of the phase information and not the very fine fringes formed by interference of object and reference beam in holography. The speckle size can be varied by adjusting the magnification M and/or the aperture ratio F=focal length/aperture=f/a of the viewing lens, as explained in Section 2.3 and is typically in the range of 5 to 50 μm. Usually a standard television camera can resolve the speckle patterns. Video processing is then used to obtain correlation fringes and perform quantitative analysis to calculate displacements.

2.5.2 Optical setup for in-plane sensitive DSPI

Figure 6 shows the schematic of a typical in-plane sensitive DSPI system which uses a phase-shifting technique for quantitative analysis.

For most work, a He-Ne laser or a diode laser is used. In the diagram, a beam splitter is used to obtain the two illuminating beams which have to be coherent with each other in order to interfere. The prism is used to compensate the optical path of one beam so that

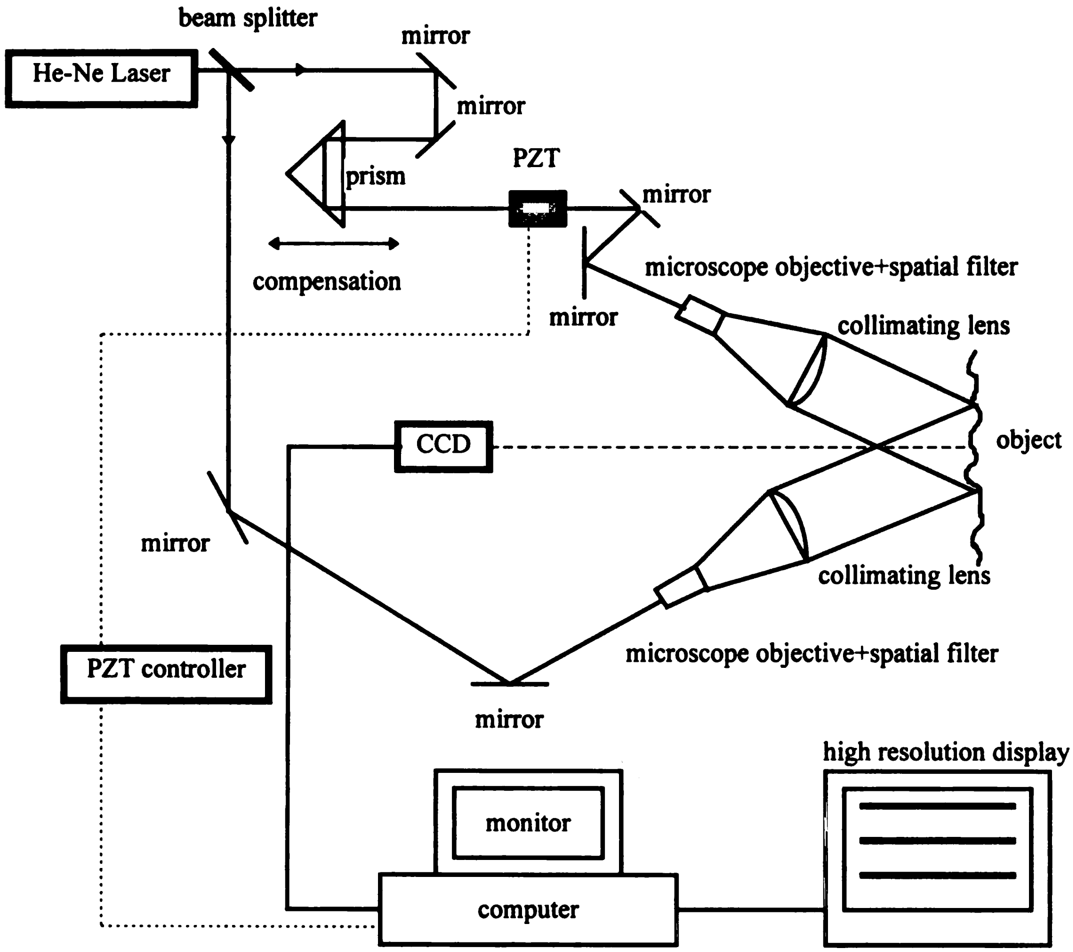

Figure 6. *Schematic of a typical in-plane sensitive DSPI system with phase shifting.*

the difference between the optical path lengths of the two beams can be made less than the coherence length of the laser light and therefore satisfy the coherence condition. The two spatial filters are used to remove extraneous optical noise. Two microscope objectives expand the beams in a spherical wavefront. The plano-convex collimating lenses then give collimated beams. This is necessary in order for the sensitivity vector to be the same over the field, as noted in Section 2.4.1. A piezo-electric transducer (PZT), controlled by a computer, is used to shift the phase of one of the two illuminating beams. This procedure is known as “phase-shifting” or “phase-stepping” technique and will be explained later in this work. It provides quantitative information on the displacement field. A CCD camera with a typical resolution of 512×512 pixels is used to record the speckle patterns, which are eventually stored in the RAM memory of a computer and processed. A high resolution monitor displays the correlation fringes.

In the out-of-plane sensitive setup of DSPI a reference beam is directed into the detector plane of the camera and only one object beam is used. In this work the attention is focused on the in-plane sensitive DSPI and the discussion is valid for the out-of-plane setup provided that one of the two illuminating (“object”) beams is substituted with a reference beam with nominally $\theta=0°$ angle of incidence on the camera detector plane (see Section 2.4.1).

2.5.2.1 The image acquisition system in DSPI

The CCD camera is used because it has wide range of linearity, low noise at low light intensity and high signal-to-noise ratio. When light falls on the CCD camera array, an output is formed in terms of a voltage signal which ideally is proportional to the image irradiance. The signal is then transferred to the computer monitor, whose brightness should vary ideally linearly with the irradiance of the original image. The word "ideally" is used to emphasize that in reality the linear range is limited. Attention should be given to camera and monitor linearities for precise measurements.

2.5.3 Fringe formation in in-plane sensitive DSPI

In DSPI at least two images of the object are taken in order to create fringes. They can be undeformed and deformed states or two different deformed states. A fringe pattern is obtained using video processing by storing the initial reference image of the object in a frame grabber and then subtracting it from the one being acquired, displaying the modulus of the result on a TV monitor. Fringes, similar to those obtained in holographic interferometry, then appear when a phase change is introduced between the reference image and the subsequent ones. The detector plate of the camera is located in the image plane of the speckle interferometer.

At the first step, the coherent combination of the two illuminating beams at a point or pixel in the CCD sensor plane results in the following intensity of light:

$$I_{before} = A_1^2 + A_2^2 + 2A_1A_2\cos\phi \tag{16}$$

where $A_1(x,y)$ and $A_2(x,y)$ are the amplitudes of the first and second object beams and $\phi(x,y)$ is the phase difference between the two beams at each point of the detector plane.

Equation (16) is obtained from Equation (8) with the simple substitution $I=A^2$ (this substitution is usually done wherever the amplitude of the electric field of the light A has to be used instead of the brightness I). This is what is called the reference image. Usually the undeformed state of the object is taken as reference. This image is digitized by a frame grabber in a computer and it is then stored in a frame buffer.

The second step consists of deforming the object by applying some kind of load and taking an image of the deformed object. The intensity of light on the CCD camera becomes:

$$I_{after} = A_1^2 + A_2^2 + 2\,A_1\,A_2\cos(\phi - \Delta\phi) \tag{17}$$

where $\Delta\phi$ is the additional phase change due to the deformation of the object. It is important to keep in mind the assumption that the deformation of the object does not displace the speckles: only a phase change within the speckles occurs; the speckle fields have to be correlated, as noted earlier in this work.

In the real-time mode, the subsequent frames are subtracted continuously from the stored reference frame. If the output camera signals V_{before} and V_{after} are proportional to the input image intensities, the subtracted signal is given by:

$$V_s = \left(V_{before} - V_{after}\right) \propto \left(I_{before} - I_{after}\right)$$
$$= 2A_1A_2\left[\cos\phi - \cos(\phi - \Delta\phi)\right] \tag{18}$$

This signal has positive and negative values. However, the television monitor will display negative values as areas of blackness, and, to avoid this loss of signal, V_s needs to be rectified before being displayed on the monitor. To do this V_s is either squared or the modulus is taken. The brightness on the monitor is then proportional to the absolute value of V_s and, point-by-point in the monitor, is given by:

$$B = KA_1A_2\left|\cos\phi - \cos(\phi - \Delta\phi)\right| \tag{19}$$

where K is a constant (2).

The resultant brightness on the monitor B varies between maximum and minimum values B_{max} and B_{min} given by:

$B_{max} = KA_1A_2$ where $\Delta\phi = (2n+1)\pi$ with n an integer→ bright point

$B_{min} = 0$ where $\Delta\phi = 2n\pi$ with n an integer→ dark point.

For any other $\Delta\phi \neq (2n+1)\pi$ or $2n\pi$, the subtraction gives a nonzero value, and the monitor shows a spot whose gray level varies accordingly to the phase change. These are called "phase fringes". Thus the monitor shows a set of fringes immersed in speckle noise and following the zones of constant phase change. The signal should be high-pass filtered to improve fringe visibility by removing low-frequency noise.

Phase fringe patterns in a plate rotated rigidly, originated by in-plane sensitive DSPI using video signal subtraction, are shown in Figures 7 and 8 for two different angles θ of rotation of the plate.

(2) *Creath (1985) observed that by subtracting the two intensities, taking the modulus squared and taking an ensemble average over many realizations of this fringe function the resultant brightness at the detector plane becomes :*

$$\langle |I|^2 \rangle = 8\langle A_1^2 \rangle \langle A_2^2 \rangle \sin^2\left(\frac{1}{2}\Delta\phi\right) \tag{20}$$

This fringe function is similar to fringes in a classical interferometer where the fringes are sinusoidally dependent on a relative phase difference. However Equation (20) depends on the phase difference between exposures rather than the phase difference between object and reference beams.

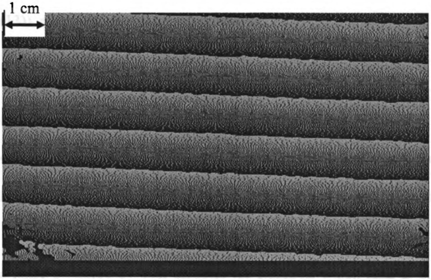

Figure 7.*Phase fringes for a rigid in-plane rotation. Angle of rotation* $\theta=1\times10^{-4}$*rad.*

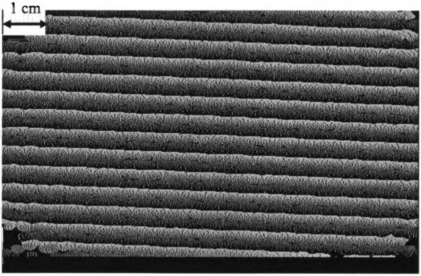

Figure 8.*Phase fringes for a rigid in-plane rotation. Angle of rotation* $\theta=2\times10^{-4}$*rad.*

The phase difference $\Delta\phi$ is related to the displacement component by the sensitivity vector, which depends on the optical geometry of the system. Recalling the relation between phase difference and displacement component for an in-plane sensitive setup (Equation (13)), a dark fringe will appear wherever:

$$d_x = \frac{n\lambda}{2\sin\theta} \tag{21}$$

Analogous relations are present for an out-of-plane sensitive setup.

Fringes in DSPI can also be created with video signal *addition*, where the light fields corresponding to the two states of the object are added at the image plane of the camera instead of being subtracted. The addition process has the disadvantage that is very sensitive to noise produced by dust particles for example, which tend to collect on the beam splitter and act as light scattering centers. This degrades the quality of the fringes. In the subtraction mode, because the noise is the same for both images, its effects cancel out in the resulting fringe pattern, and, therefore, the subtraction fringes are qualitatively better.

2.6 Automatic quantitative fringe analysis

2.6.1 Introduction

Interferometric fringes are a map of a warped wavefront which is in turn indicative of something useful, such as components of displacement or the shape of a surface. To interpret these fringes, one can count the fringes and perform other calculations using some parameters depending on the particular technique used. The results are then interpolated between the fringes to give the variable of interest anywhere in the field.

This process presents some difficulties. It is slow and tedious. Sometimes there are not enough fringes to provide accurate results from interpolation, especially when the spatial gradients of the variable of interest are high. Although techniques of fringe multiplication have been developed, this is not the best way to obtain an accurate map over the field of the variable of interest. Moreover, in the case of DSPI, the correlation fringes are not clearly defined because they are composed of variations in speckle contrast (see Figures 7 and 8). They are good for qualitative measurements but have not produced good quantitative results, since it is hard to determine the fringe centers and the fringe spatial resolution is generally pretty low.

A technique of fringe multiplication in DSPI has been developed by Floureux (1993). He subdivided the total deformation into small increments, recorded the phase fringes for each increment and digitally added them together to obtain fringes representing the total deformation. But the point is that multiple fringes don't actually represent a higher amount of information than regular fringes, since theoretically even a low-frequency phase-fringe pattern contains detailed local displacement information in the form of phase values: this is the property that is used in phase-shifting techniques.

Quantitative data can be obtained using phase-shifting interferometry (PSI). The whole point is purposely shifting the phase of one beam in the interferometer with respect to the other. The phase of the test wavefront relative to the reference wavefront can be simply calculated form the interferogram intensities measured for multiple phase shifts. This phase measurement technique has been known for almost thirty years (Carre' 1966, Creath 1985).

In speckle interferometry the phase maps are calculated from sets of phase-shifted intensity data taken before and after the deformation and then combined to produce the phase of the difference between exposures. Each set of phase-shifted intensity data is obtained in the same way as PSI. To find the phase of the object deformation, the phases of the speckle patterns before and after the deformation are simply subtracted. The deformation of the object is then calculated from the phase data using the sensitivity vector theory.

2.6.2 The phase-shifting technique

Recalling Equation (8), which expresses the irradiance resulting from interference of two speckle patterns in an in-plane sensitive setup at any image point on the detector plane of the interferometer, it can be written:

$$I(x,y) = I_1(x,y) + I_2(x,y) + 2\sqrt{I_1(x,y)\,I_2(x,y)}\cos\phi \tag{22}$$

where $I_1(x,y)$ and $I_2(x,y)$ are the light intensities of, respectively, beam 1 and beam 2, and ϕ is the phase difference between the two waves contributing to point P in the image.

For convenience, equation (22) can be rewritten in the following form:

$$I(x,y) = I_0(x,y)\left[1 + \gamma_0 \cos\phi(x,y)\right] \tag{23}$$

where the intensity $I_0(x,y)$ is the sum of the intensities of the two illuminating beams ($I_0=I_1+I_2$) or the dc intensity, $\gamma_0(x,y) = \dfrac{2\sqrt{I_1 I_2}}{I_1 + I_2}$ is the modulation depth of the intensity in the interference fringe pattern, and $\phi(x,y)$ is the phase difference between the two illuminating beams.

In equation (23) there are three unknowns, namely I_0, γ_0 and ϕ . Therefore a minimum of three intensity measurements (called buckets) at known values of phase shifts is needed to calculate the phase $\phi(x,y)$.

If a known phase shift α_i is introduced in one of the beams in the inteferometer, equation (23) becomes:

$$I(x,y) = I_0(x,y)\left[1+\gamma_0 \cos\left[\phi(x,y)+\alpha_i\right]\right] \tag{24}$$

where α_i is the average value of the relative phase shift for the ith exposure.

The present discussion is made for the in-plane setup i.e. double illumination. For the out-of-plane sensitive setup, i.e. single illumination and reference beam, the concepts are the same and the reference beam is the one usually shifted by known amounts.

Equation (24) is sometimes written in the literature (e.g. Morimoto and Fujisawa 1993 and 1994, Perry and McKelvie 1993) as:

$$f(x,y) = a(x,y)\cos\left[\phi(x,y)+\alpha\right] + b(x,y) \tag{25}$$

where f(x,y) is the brightness distribution, a(x,y) is the amplitude of brightness or modulation strength, b(x,y) is the average brightness or background intensity variation, ϕ(x,y) is the phase that one has to analyze at any point (x,y) on the fringe pattern and α is the amount of the phase shift. A schematic of the resulting brightness distribution on a line of a fringe pattern is shown in Figure 9.

There are two ways of introducing phase changes, as shown in Figure 10 :

1) Discrete phase steps are used so that the phase is constant during the integration time of each TV-frame (remember that detectors always measure time-averaged irradiance). This is called *phase-stepping.*

2) The phase is linearly and continuously shifted during the integration time of each TV-frame. This is called *phase-integration* or *phase-shifting.*

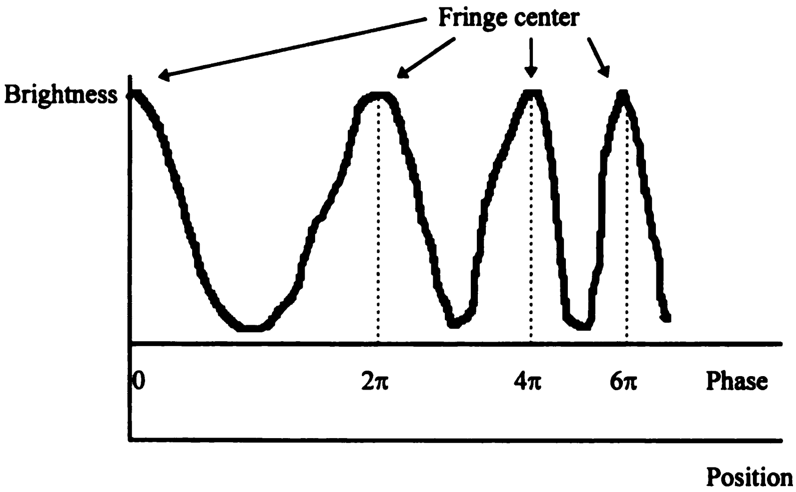

Figure 9. *Brightness and phase distribution on a line of a fringe pattern.*

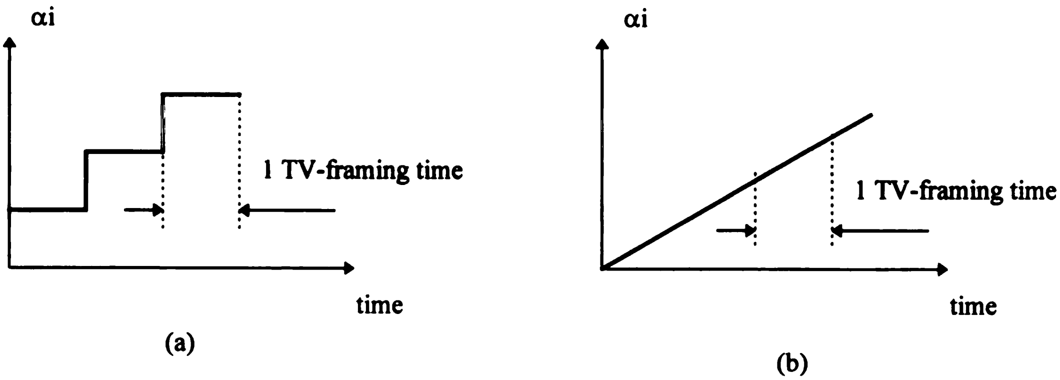

Figure 10. *(a) phase-stepping technique; (b) phase-integration technique.*

In phase-stepping, α_i in equation (24) is a constant for each ith bucket. In phase-integration instead, αi is the average phase shift during the ith TV frame integration time.

In phase-integration, the average recorded intensity integrated during one TV frame is given by (Greivenkamp 1984):

$$I_i(x,y) = \frac{1}{\Delta}\int_{(\alpha_i-\Delta/2)}^{(\alpha_i+\Delta/2)} I_0(x,y)\left[1+\gamma_0 \cos\left(\phi(x,y)+\alpha(t)\right)\right]d\alpha(t)$$

$$= I_0(x,y)\left\{1+\gamma_0\left(\frac{\sin\Delta/2}{\Delta/2}\right)\cos\left(\phi(x,y)+\alpha_i\right)\right\} \qquad (26)$$

where Δ is the amount of *change* in relative phase of the beams *within each exposure*. The integration over Δ makes this expression applicable for any phase-shifting technique. For the case of phase stepping it is Δ=0.

The term

$$\gamma(x,y) = \gamma_0(x,y)\left(\frac{\sin\Delta/2}{\Delta/2}\right) \qquad (27)$$

is the recorded intensity modulation or fringe visibility.

The only difference between phase stepping and phase integration is that the latter yields a smaller modulation in the measured interference pattern per bucket than the former (Van Wingerden, Frankena and Smorenburg 1991). In other words, the fringe visibility in phase integration is lower than in phase stepping. This is clearly seen by noting that γ(x,y) is always smaller than γ_0(x,y) in equation (27). The two terms coincide only for Δ=0.

For Δ=0 equation (26) becomes equation (24) and the term γ(x,y) coincides with γ_0(x,y). Phase stepping is therefore a simplification of the integration method. For $\Delta=2\pi$ there would be no modulation intensity. In order to have modulation of the intensities as the phase is shifted, the phase shift per exposure needs to be between 0 and π.

2.6.3 Some phase extraction algorithms

As stated earlier, a minimum of three buckets has to be recorded in order to calculate the phase distribution for a given interferometric fringe pattern. Many phase calculation algorithms have been developed. They generally use different numbers N of buckets and different amounts of phase shifts α_i. The same formulas for calculation of phase from the buckets apply in the phase stepping and the phase integration techniques. Some of the common algorithms used are the following:

(1) Three buckets (90): N=3, $\Delta=\pi/2$, shifts $\alpha= \pi/4$, $3\pi/4$, and $5\pi/4$.

The three intensity measurements are expressed as (Creath 1988):

$$I_1(x,y) = I_0(x,y)\left(1+\gamma\cos\left[\phi(x,y)+\frac{1}{4}\pi\right]\right) \tag{28}$$

$$I_2(x,y) = I_0(x,y)\left(1+\gamma\cos\left[\phi(x,y)+\frac{3}{4}\pi\right]\right) \tag{29}$$

$$I_3(x,y) = I_0(x,y)\left(1+\gamma\cos\left[\phi(x,y)+\frac{5}{4}\pi\right]\right) \tag{30}$$

The phase at each point is given by:

$$\phi(x,y) = \arctan\left(\frac{I_3(x,y)-I_2(x,y)}{I_1(x,y)-I_2(x,y)}\right) \tag{31}$$

The intensity modulation is:

$$\gamma(\mathrm{x,y}) = \frac{\sqrt{[\mathrm{I}_1(\mathrm{x,y})-\mathrm{I}_2(\mathrm{x,y})]^2+[\mathrm{I}_2(\mathrm{x,y})-\mathrm{I}_3(\mathrm{x,y})]^2}}{2\mathrm{I}_0} \tag{32}$$

From equation (27), for $\Delta=\pi/2$ it is: $\gamma=0.9\gamma_0$. This means that with a phase-integration method the fringe visibility reduction with respect to the phase-stepped method in this case is 10%.

(2) Three buckets (120): N=3, $\Delta=2\pi/3$, shifts $\alpha= -2\pi/3$, 0, and $+2\pi/3$.

In this case the phase is given by:

$$\phi(x,y) = \arctan\left(\frac{\sqrt{3}(I_3(x,y) - I_2(x,y))}{2I_1(x,y) - I_2(x,y) - I_3(x,y)}\right) \tag{33}$$

The intensity modulation is:

$$\gamma(x,y) = \frac{\sqrt{3[I_3(x,y) - I_2(x,y)]^2 + [2I_1(x,y) - I_2(x,y) - I_3(x,y)]^2}}{2I_0} \tag{34}$$

For this case, $\gamma=0.83\gamma_0$.

(3) Four buckets (90): N=4, $\Delta=\pi/2$, shifts $\alpha=0$, $\pi/2$, π and $+3\pi/2$.

This is the most common algorithm. The intensities for the four exposures are given by:

$$I_1(x,y) = I_0(x,y)\left(1 + \gamma\cos[\phi(x,y)]\right) \tag{35}$$

$$I_2(x,y) = I_0(x,y)\left(1 + \gamma\cos\left[\phi(x,y) + \frac{\pi}{2}\right]\right) \tag{36}$$

$$I_3(x,y) = I_0(x,y)\left(1 + \gamma\cos[\phi(x,y) + \pi]\right) \tag{37}$$

$$I_4(x,y) = I_0(x,y)\left(1 + \gamma\cos\left[\phi(x,y) + \frac{3\pi}{2}\right]\right) \tag{38}$$

The phase is given by:

$$\phi(x,y) = \arctan\left(\frac{I_4(x,y) - I_2(x,y)}{I_1(x,y) - I_3(x,y)}\right) \tag{39}$$

The modulation is then expressed as:

$$\gamma(x,y)=\frac{\sqrt{[I_4(x,y)-I_2(x,y)]^2+[I_1(x,y)-I_3(x,y)]^2}}{2I_0} \tag{40}$$

Here, γ=0.9γ_0.

It is useful to notice that the reduction in fringe visibility in the case of phase-integration is pretty small, and this leads one to think that this method is generally better than the phase-stepped technique, which is slower because a time delay is required between the steps to damp out any oscillation in the PZT and settle down the shifted beam.

(4) Carre' technique .

In all the previous algorithms the amounts of phase shift α has to be known. The knowledge of this parameter requires a precise calibration of the phase shifter, which is not an easy task to perform. A technique which is independent from the magnitude of the phase changes was developed by Carre' (1966). He proposed that the phase is shifted by a constant value α between consecutive intensity measurements, assuming the phase shift linear with time.

The expression of the phase is:

$$\phi(x,y)=\arctan\frac{\sqrt{[3(I_2-I_3)-(I_1-I_4)][(I_2-I_3)+(I_1-I_4)]}}{(I_2+I_3)-(I_1+I_4)} \tag{41}$$

An advantage of the Carre' technique, other than the obvious that the phase shifter doesn't need to be calibrated, is that it can work with converging or diverging beams where the amount of phase shift varies across the beam. The disadvantage is that the phase calculation is more complicated.

2.6.4 Comparison of algorithms

Van Wingerden *et al.* (1991) give a comprehensive survey on the possible errors occuring in the different phase measurement techniques. As sources of system errors, they consider light source instability, imperfect beam phase shifting, mechanical vibrations, nonlinearity of the detector and quantization of the detector signal. They conclude that if the system is not well calibrated and 4 buckets are measured, the Carre' formula gives the best error reduction. If the system is properly calibrated, the most accurate formula is that for 4 buckets. For phase-stepping, however, the measurement error still decreases (to a nonvanishing asymptotical value) for an increasing number N of buckets. Therefore, techniques which use more than 4 buckets (e.g. 5 buckets) are preferable. The disadvantage is, of course, an increase in computational analysis. A large number of buckets reduces also the effect of the random phase-shift errors.

Cloud (1995) points out that the 4 bucket technique is the best for eliminating effects caused by second- and third-order detection nonlinearities. He also notes that there is little difference in results between phase-stepping and phase-integration. Only in the case of non-linear phase-shift errors is the integration method superior.

2.6.5 Phase-shifting devices

The most common way of performing the phase shift in a beam is the piezoelectric transducer (PZT) mirror. Other ways have been used, such as tilting glass plate (Creath 1988) or polarization phase-shift device (Jin and Tang 1992). In optical fiber speckle interferometry, the phase shifting is usually performed by stretching the optical fiber wrapped around a PZT (e.g. Joenathan and Khorana 1992).

2.6.6 Phase unwrapping

The formulas given in Section 2.6.3 for the calculation of the phase $\phi(x,y)$ involve an arctan function. Therefore, they yield results "modulo π". This means that the calculated phase has an uncertainty of $n\pi$, where n is an integer.

The first step is to obtain a phase "modulo 2π". This is done considering the sign of the numerator and the denominator of the tangent function, i.e. the sine and cosine functions respectively .

$$\tan\phi = \frac{\sin\phi}{\cos\phi} = \frac{Num}{Den} \tag{42}$$

Doing this, one can exactly locate the phase ϕ in one of the four quadrants, as shown in Figure 11. This method can be applied to all the algorithms treated earlier, except for the Carre', which involves a more complicated process (Creath 1985).

A similar procedure is commonly used for data reduction in strain gage rosette analysis. In this case an arctan function is involved for the calculation of the orientation of the principal strains with respect to the rosette axes.

After evaluating the phase modulo 2π, the phase ambiguities are then removed by comparing the values between two adjacent detector elements (phase unwrapping). If the absolute difference between two adjacent detector elements exceeds a certain threshold (which is usually π, for reliable removal of discontinuities) a fringe edge is detected and an offset equal to a multiple of 2π is added or subtracted until this difference is less than π. A fringe order number N is then recorded such that the phase at that point is given by "old phase+$2N\pi$". The deformation phases are then usually displayed as different gray levels (normally, gray level 255 is equal to one fringe period). This calculation restricts the total number of resolvable fringes, in other words the sensitivity of the system, since the phase difference between adjacent points should not vary by more than π (Chang *et al.* 1985).

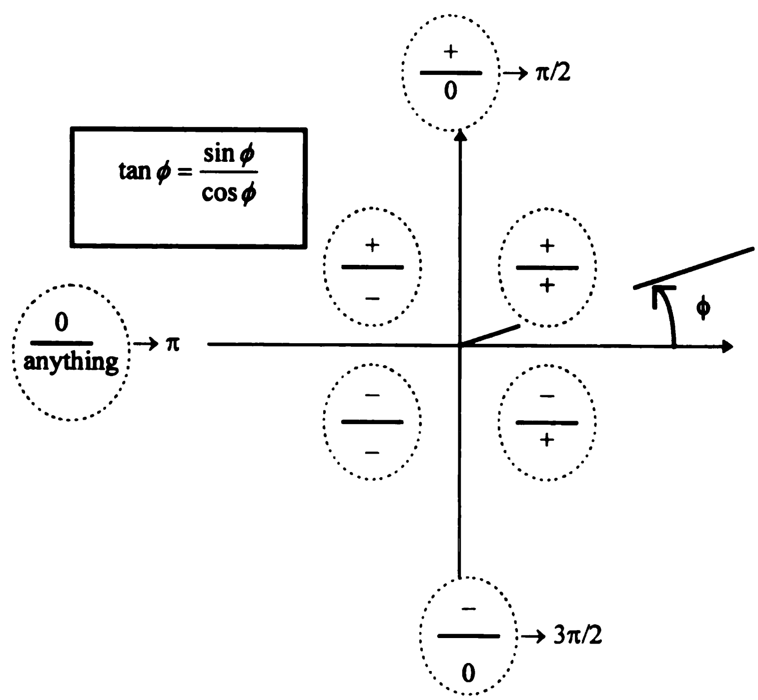

Figure 11. *Determination of the phase "modulo 2π"*.

Figure 12 shows a schematic of a phase unwrapping.

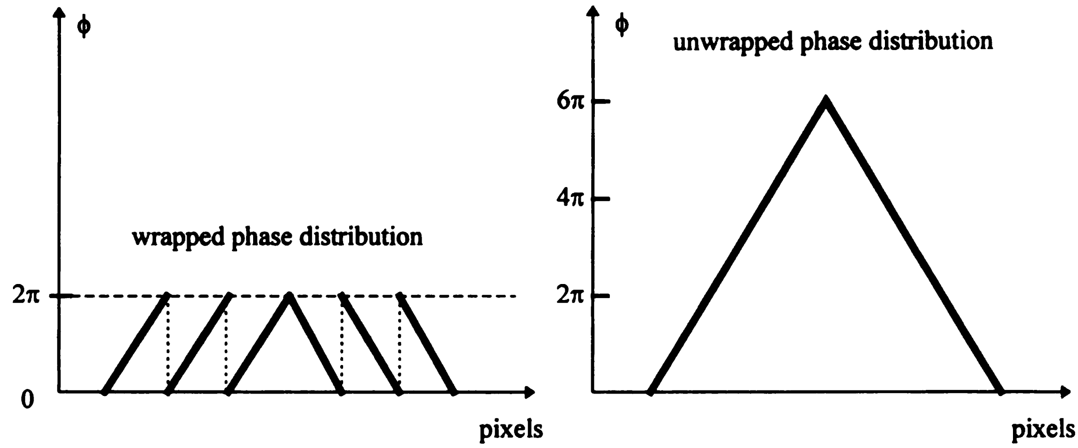

Figure 12. *Schematic of phase unwrapping.*

This calculation needs a point in the detector array to start the unwrapping. The final phase map is therefore relative to this reference location. The only case where it yields absolute phase values is when the chosen starting reference point is a fixed point in the object. Sometimes it is not possible to locate a fixed point in a structure and the result is only relative to a point. Usually the starting point is chosen to be in one of the four corners or at the center of the image (e.g. Vrooman and Maas 1991); the detector array is then scanned point by point until the whole image is unwrapped. Region by region unwrapping is also possible.

2.6.7 Sources of error in phase measurement and remedies

Noise, low modulation, physical holes and speckle decorrelation can induce errors in the phase unwrapping. Good regions, e.g. regions with small phase gradients, low noise and correlated speckles, should be unwrapped before other regions. Data-conditioning is necessary before performing the unwrapping. Operations like detection of low-modulated pixels, median filtering and smoothing filtering are very useful for this purpose.

Noise can arise from particles in the air and in the optical components, electronic noise and round-off-errors in the frame grabber system. The total noise term has usually a continuous spectrum with a predominance of low frequency component (Vikhagen 1991).

Low modulation is a fundamental problem in phase shifting technique (Creath, Cheng and Wyant 1985). This problem is schematized in Figure 13.

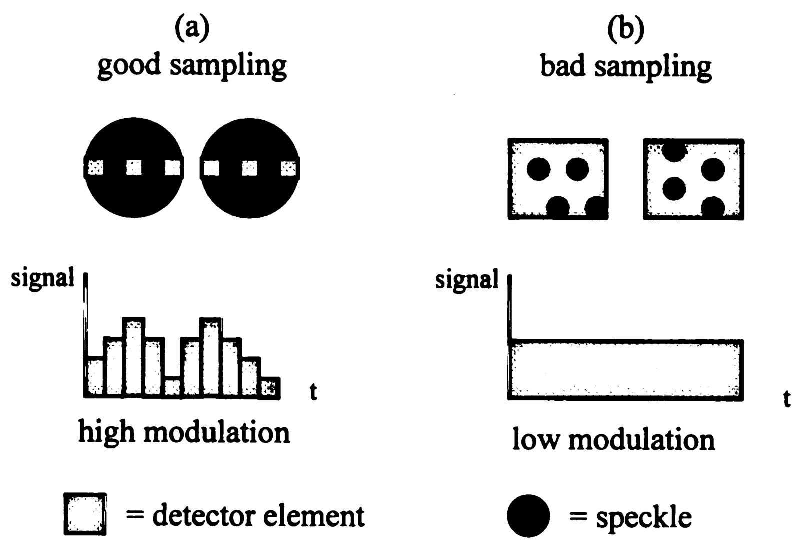

Figure 13. *Sampling of a speckle pattern with finite-sized detector elements. (a) good sampling; (b) bad sampling.*

Because speckle is sampled with a finite-sized detector element, the measured intensity is an average over the detector area. To resolve the speckles in the image plane, the f/No. of the viewing system is set to adjust the speckle size according to the pixel size. Yet, for only one speckle to influence each detector and therefore for having perfect sampling of the speckle pattern, the detector size would have to be about a tenth of the speckle size (Creath 1985). If the aperture were made this small, very little light would get through. With a detector element of the same size as the speckle, the intensity will not modulate during phase shifting as it would for point sampling. This is due to averaging over a pixel with more than one speckle influencing it. This problem could be corrected using point detector elements.

When the modulation $\gamma(x,y)$ at a pixel as the phase is shifted is less than some γ_{min}, the pixel is considered "bad" and is usually removed from the data sets before performing any phase calculation. γ_{min} is called modulation threshold and is set by the user.

Median filtering is an operation which takes all the data points contained within a window, sorts them until the median is found and then replaces the values of the center of the window with the calculated median. The window is then moved by one pixel and the procedure is repeated until the whole array has been processed. The size of the window depends on the context. This technique is good in filling up bad data points but does not change the pixel values with phase errors.

Smoothing filtering is a routine used to smooth data points. It compares each data point to usually eight nearby pixels in the form of a plus sign. If most of the nearby points have phase values different form the center pixel, its value is replaced with the average of the good nearby pixels, otherwise it is left alone. If the dimension of the array smoothing window is n×n, the random noise is reduced by a factor of 1/sqrt(n).

Detector nonlinearity is another potential source of error in phase measurement. For CCD (charge-coupled-device) detectors the nonlinearity is negligible ($\gamma \approx 1$), but for vidicon tubes the nonlinearity can be considerable (e.g. $\gamma = 0.7$). The measurement errors caused by detector nonlinearity can be approximated linearly as a function of the intensity deviation (difference between measured intensity and actual light intensity at the detector) (Van Wingerden *et al.* 1991).

Environment disturbances such as air turbulence and floor vibration can also cause measurement errors. A simple check with live correlation fringes can give one a feeling of the influence of these factors for a particular experiment. When possible, tests are carried out on vibration-isolated tables.

2.6.8 Issues on spatial resolution in DSPI

Phase-shifting techniques increase sensitivity and spatial resolution of the measurements in DSPI. The *spatial resolution limit*, i.e. the resolution of small sized details in the deformation pattern and the *sensitivity limit* (or signal resolution), i.e. the resolution of the magnitude of deformations/displacements of the object surface, are connected to one another. As an example, smoothing of the images results in an increase in sensitivity but a decrease in spatial resolution.

To investigate the spatial resolution of a DSPI system, one can test an object which gives a periodic deformation pattern (Vikhagen 1991): the resolution limit is then defined by the minimum resolved spatial period measured in units of the pixel distance. The theoretical limit for spatial resolution is, however, given by the pixel size in the frame grabber system. The frame grabber boards normally used in PC's for DSPI have a spatial resolution of 512×512 pixels. This theoretical limit represents a deformation pattern with a spatial period of two pixel distances and can be achieved only if the spatial resolution of the camera is equal to or better than the spatial resolution of the frame grabber board in the computer.

Noise has a big influence on resolution limits of the DSPI system. Because of the noise factor, it is unrealistic to operate with a spatial resolution limit of one pixel size for a deformation experiment: the high spatial frequency components of the noise may then give large errors in the phase unwrapping. In order to reduce the effect of noise and to increase the signal-to-noise ratio (SNR), the image is smoothed before proceeding for the phase calculation as explained in Section 2.6.7. The smoothing inevitably reduces the spatial resolution of the measurements, so the point is to choose the amount of smoothing so that one gets a satisfactory signal-to-noise ratio without losing too much resolution.

2.6.9 The displacement calculation

To find the deformation of an object, the phases calculated with the phase-shifting technique *before* and *after* the displacement are subtracted from one another. They are unwrapped after performing the subtraction.

$$\Delta\phi(x,y) = \phi_{before} - \phi_{after} = \phi(x,y) - \left[\phi(x,y) - \Delta\phi(x,y)\right] \tag{43}$$

The phase variation $\Delta\phi(x,y)$ is then related to the displacement component by Equations (4) and (12) for an out-of-plane and an in-plane sensitive setup respectively. In the in-plane arrangement, for example, the displacement is calculated as:

$$d_x(x,y) = \frac{\Delta\phi(x,y)\lambda}{4\pi\sin\theta} \tag{44}$$

where the symbols are explained in Section 2.4.2.

2.7 Advantages and disadvantages of DSPI

Advantages of DSPI are:

1) Computer controlled fast data acquisition (1/30 sec. per frame), signal processing and graphical result presentation.

2) Precise quantitative analysis with the use of optical phase measurement techniques such as phase-shifting, which give spatial resolutions on the order of a few pixels and high sensitivity, even in cases where only few fringes are observed.

3) Since typically only 1/30 sec. is needed to record a frame of specklegram, the vibration isolation is relaxed a bit. Furthermore, ideally an acceptable vibration should have amplitude smaller than the speckle size and this is always a smaller restriction compared to the requirement for vibration isolation in holographic interferometry. This means that the system does not require the highly stable environment necessary for conventional holographic interferometry.

4) The system can be used in brightly lighted conditions. No dark room is needed.

5) No photographic processing, optical spatial filtering or plate relocation are needed; material cost is then very low.

6) The technique is non-invasive.

Disadvantages of DSPI are:

1) Limited maximum range of measurements (~50 μm) without special measures.

2) Low spatial resolution of correlation fringes. Necessity of phase measurement techniques when quantitative analyses are needed.

3) Sensitive to rigid-body motions.

4) Usually, necessity of plane illuminating wave fronts which implies difficulty in studying large areas.

CHAPTER III

EXPERIMENTAL PROCEDURE: PRELIMINARIES

3.1 Introduction

In this study Digital Speckle Pattern Interferometry (DSPI) was used to study mechanically fastened composites. High precision strain measurements were requested. In order to accomplish this, a phase-stepping algorithm had to be used. The setup employed throughout this work was the in-plane sensitive one, and it is schematized in Figure 6, page 29. From this point on we will always refer to this setup.

At the first stage, three goals had to be accomplished:

1) A commercial four-bucket phase-stepping algorithm by Ealing Electro-Optics was available. This algorithm was designed by the company to be used in an out-of-plane sensitive DSPI setup. In other words, the software displayed values of out-of-plane components of displacement. This software wasn't editable, being already compiled. The first goal was therefore understanding how such an algorithm could be used in an in-plane sensitive DSPI setup. This basically turned into a "calibration" problem.

2) The system had to be "set-up", in terms of aperture ratio of the viewing system, image filtering, etc. Also sensitivity and maximum range of the measurements had to be determined.

3) The measured displacements had to be converted to strain values. The procedures to convert displacements into strains are always a challenging part in this kind of study,

because it is easy to introduce errors. The third goal was therefore to make sure that the procedure used to get strains from displacements was accurate enough for the purposes of the present research.

3.2 Calibration of the technique

The commercial phase-stepping algorithm involved was a four-bucket phase-stepping (Section 2.6.3). It was designed to be used along with a commercial unit for out-of-plane DSPI by Ealing Electro-Optics. Four images of the undeformed object and four images of the deformed object were taken at different phase-shifts. The program showed then the out-of-plane component of the displacement of the object as 2D and 3D plots on the computer monitor.

The idea that this result could also be used in an in-plane setup after some modification was the following. In any phase-stepping or phase-shifting algorithm, the calculation of the phase does not depend on which kind of setup (in-plane sensitive or out-of-plane sensitive) is used. The phases "before" and "after" the deformation are simply subtracted to obtain the phase $\Delta\phi(x,y)$ due to the deformation (see Section 2.6.9). The phase $\Delta\phi(x,y)$ is then related to the displacement component by equations which depend on the optical setup. Namely, for an out-of-plane sensitive setup it is:

$$d_z(x,y) = \frac{\Delta\phi(x,y)\lambda}{2\pi\left(\cos\theta_i + \cos\theta_v\right)} \tag{45}$$

where λ is the wavelength of illumination and θ_i and θ_v the angles of illumination and viewing with respect to the surface normal.

For an in-plane sensitive setup it is:

$$d_x(x,y) = \frac{\Delta\phi(x,y)\lambda}{4\pi \sin\theta} \tag{46}$$

where λ is the wavelength of illumination and θ the illumination angle with respect to the surface normal.

Because of the phase-unwrapping procedure, the results obtained by a phase-calculation algorithm are not absolute values, but relative to the point were the phase unwrapping itself starts, as explained in Section 2.6.6. It can be written:

$$\Delta\phi_{calc}(x,y) = \Delta\phi_{abs}(x,y) - \Delta\phi_{ref}(x_0,y_0) \tag{47}$$

where: $\Delta\phi_{calc}(x,y)$ is the calculated phase due to the deformation, point by point in the specimen;

$\Delta\phi_{abs}(x,y)$ is the absolute phase due to the deformation, point by point in the specimen;

$\Delta\phi_{ref}(x_0,y_0)$ is the phase due to the deformation at the reference point (x_0,y_0) in the specimen where the unwrapping procedure starts.

This is generally true unless the starting point is a fixed point in the object. In our pin-loaded composite experiment any point in the pin was a fixed point; the pin being "infinitely" rigid, it remained static during deformation. But starting the unwrapping from these points would have caused large errors, because the pin was a low modulated region of the image. Therefore, in the experiments performed in the present work, the displacements obtained were always relative to a point.

From equations (45) and (47), the calculated out-of-phase component of the displacement can be expressed as:

$$d_{zcal}(x,y) = \frac{\Delta\phi_{cal}(x,y)\lambda}{2\pi\left(\cos\theta_i + \cos\theta_v\right)} =$$

$$= \frac{\Delta\phi_{abs}(x,y)\lambda}{2\pi\left(\cos\theta_i + \cos\theta_v\right)} - \frac{\Delta\phi_{ref}(x_0,y_0)\lambda}{2\pi\left(\cos\theta_i + \cos\theta_v\right)} \tag{48}$$

From equation (46), the absolute in-plane component of the displacement can be expressed as:

$$d_{xabs}(x,y) = \frac{\Delta\phi_{abs}(x,y)\lambda}{4\pi\sin\theta} \tag{49}$$

Combining equations (48) and (49) we get:

$$d_{xabs}(x,y) = \frac{\cos\theta_i + \cos\theta_v}{2\sin\theta} d_{zcalc}(x,y) + \frac{\Delta\phi_{ref}(x_0,y_0)\lambda}{4\pi\sin\theta} = A\, d_{zcalc}(x,y) + B \tag{50}$$

where: $$A = \frac{\cos\theta_i + \cos\theta_v}{2\sin\theta} \tag{51}$$

$$B = \frac{\Delta\phi_{ref}(x_0,y_0)\lambda}{4\pi\sin\theta} \tag{52}$$

Equation (50) relates the out-of-plane component of the displacement calculated by the commercial phase-stepping algorithm to the absolute in-plane component of the displacement.

A and B are constants over the specimen. Their expressions are given in equations (51) and (52). The multiplying constant A is some kind of "calibration" constant; it only depends on the optical setup used, namely on illumination and viewing angles. The additive constant B depends also on the reference point in the specimen where the phase unwrapping starts.

Nevertheless, in the subsequent calculation of strains, the displacement maps are differentiated along certain directions on the specimen and therefore the additive constant B in equation (50) does not influence the strain values, which are always representing "absolute" quantities (not relative to the value at a reference location). Since the results of this work are in terms of strains/stresses, we can simply ignore the constant B in this discussion and think always in terms of absolute quantities.

Equation (50) can be therefore simply written as:

$$d_X(x,y) = A d_Z(x,y) \tag{53}$$

The knowledge of the "calibration" constant A made it possible to convert the results given by the commercial software, namely $d_z(x,y)$, into the needed quantities, namely $d_x(x,y)$, for the in-plane sensitive setup.

The determination of A from equation (51) would have involved the measurement of the angles θ_i, θ_v and θ, which is not an easy task to perform with a high degree of accuracy. Furthermore, measurement errors would be amplified in the subsequent calculation of strains. For these reasons, instead of performing a "theoretical" calibration according to equation (51), an "overall" calibration was performed to calculate the value of the constant A which had to be used in the setup. For this purpose, known values of in-plane displacements were induced using a rigidly-rotating plate equipped with a micrometer accurate to within 0.0001", as shown in Figure 14. This device was developed by Cloud (1975) for use in quantitative speckle photography.

This experiment gave horizontal correlation fringes (loci of constant component d_x of displacement), as expected for small rotations of the plate (Appendix B). Figure 15 illustrates the formation of the fringes.

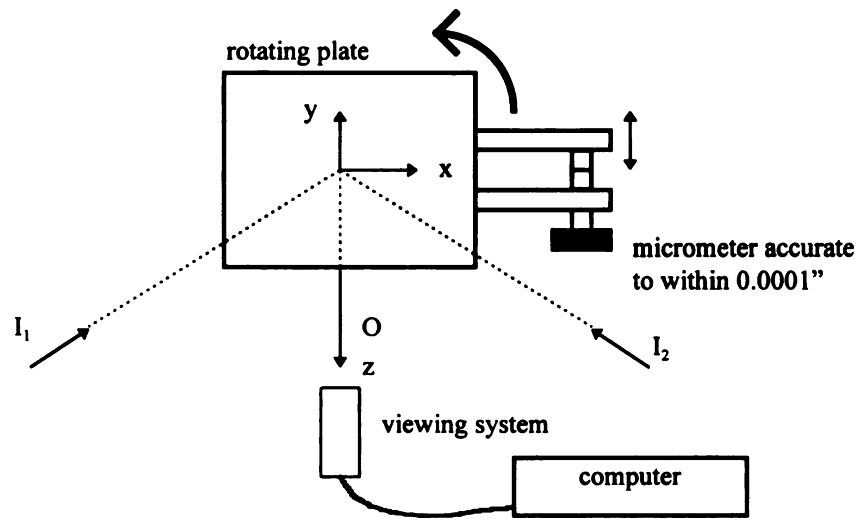

Figure 14. *In-plane rotating plate used to induce known values of d_x*

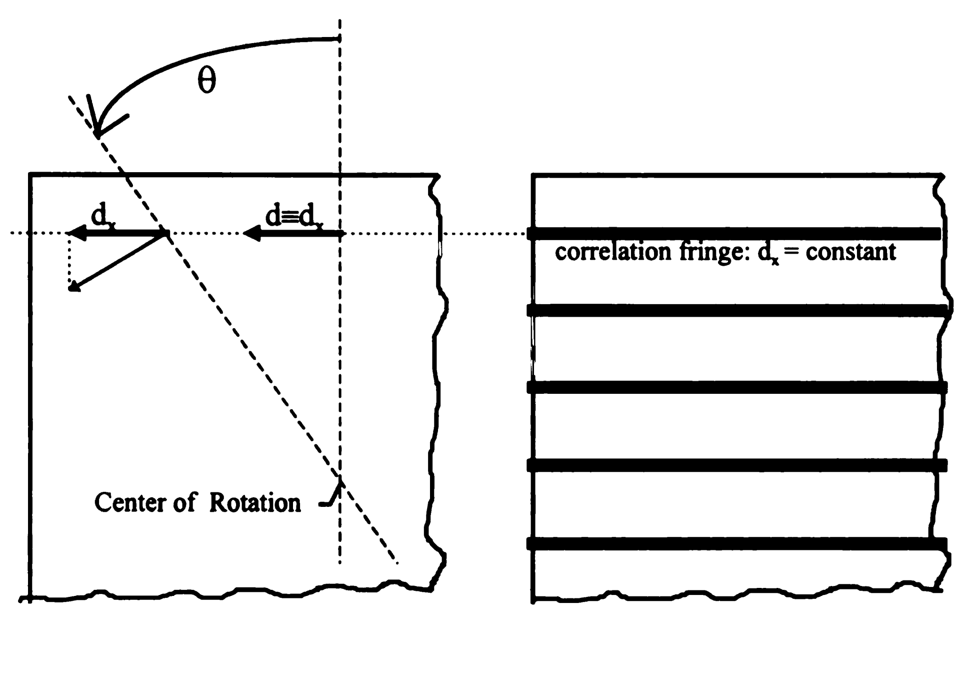

Figure 15. *Formation of fringes for rigid in-plane rotation of a plate.*

Figures 7 and 8 in Section 2.5.3 show the correlation fringes obtained in this experiment for two different angles of rotation $\theta=1\times10^{-4}$ rad and $\theta=2\times10^{-4}$ rad.

Values of the displacement obtained by the commercial algorithm were then compared to the known values of induced displacements. As expected, they differed by a multiplication constant and an additive constant. The value of the multiplication constant A was easily determined by this comparison, providing a satisfactory calibration of the system.

Its worth noting that in this "overall" calibration no measurements of optical angles were involved.

3.3 Experimental apparatus and system "setup"

The optical system used was presented in Figure 6 (Section 2.5.2). The light source was a Helium-Neon laser by Siemens with a maximum output of 15 mW. Its wave length was 0.6328μm.

The imaging system (see Figure 5, Section 2.4.2) consisted of a CCD 512×512 pixel resolution black and white video camera and a viewing lens. The camera was connected to a 12 volt DC power supply. After different tests, the optimum aperture ratio of the viewing system was determined to be F=f/a=4. This gave maximum speckle contrast and was appropriate for the light source power used. This aperture ratio was used throughout the work. The focal length of the viewing lens was f=50mm and the magnification M=1:1.4. The camera detector array was connected to a Data Translation DT2851 frame-grabber card installed in a 286 Hewlett Packard Personal Computer, where the image processing was performed. A high resolution monitor was used for result display.

The expanding lenses used for the two illuminating beams were two microscope objectives with magnification M=40X and numerical aperture 0.65. To remove the optical noise, two spatial filters with pin hole diameter equal to 10 μm were also employed. After being expanded, the two illuminating beams were collimated by two plano-convex lenses with focal length f=305 mm and diameter D=89 mm. The incidence angle of the illuminating beams (angle θ in Figure 5) was $\theta=30°$. This angle determined the sensitivity of the correlation fringes.

With this system we were able to investigate a circular area on the specimen of approximately 80 mm of diameter. All the specimens used had to be coated with a matte white paint in order to have a reasonably diffusive surface. All the experiments were performed on an optical table with pneumatic isolator legs by Technical Manufacturing Corporation (TMC).

The rotating plate experiment discussed in Section 3.2 was also used to determine sensitivity, maximum range of the measurements and spatial resolution of the correlation fringes.

The experimental sensitivity of the correlation fringes was found to be ≈0.675μm/fringe. The theoretical sensitivity was calculated to be 0.6328μm/fringe through the use of equation (14). The small difference between theoretical and experimental sensitivity is due to approximations in the value of the angle of illumination θ used in equation (14). Nearly zero sensitivity was observed for the other two components of the displacement, namely d_y and d_z.

The maximum range of the measurements was determined by inducing large rotations in the plate until speckle decorrelation occurred, which determined the disappearance of the correlation fringes. This maximum measurable displacement was determined to be $d_{xmax} \approx 17 \mu m$. The theoretical upper limit of the measurement range is determined by the pixel size in the detector plane and the speckle size on the object, which is in turn dependent on aperture ratio and magnification of the viewing system (see Section 2.3). For our case, the theoretical maximum range of the measurements calculated from equation (2) was $d_{xmax}=7.4 \mu m$. It is not clear why the difference with the experimental value is so large. Surely the speckle phenomenon is a random one in itself, being originated by random light scattering from an object surface. Therefore it is believed that the theoretical speckle diameter given in equation (2) does not truly represent the dimension of each speckle in a specklegram. Also, imprecision in determination of the values of viewing system aperture ratio and magnification used in equation (2) contributes to this mismatch. The experimental result was considered more reliable than the theoretical one.

In the following experiments we never approached speckle decorrelation caused by too large displacements; the deformation of the test specimens was always within the measurable range.

The maximum spatial resolution of the correlation fringes was ~ 1 fringe per millimeter of the object surface and we were able to observe up to 25 fringes for a $\sim 19 \times 19$ mm^2 area of the object.

Before performing the phase calculation, the images were filtered with a 5×5 pixel array smoothing window at least three times. Each filtering took about 22 seconds. This filtering provided a good signal-to-noise ratio without losing too much signal spatial resolution. A pixel modulation threshold (see Section 2.6.7) for the minimum modulation acceptable for a pixel was set, so that pixels with low modulation were ignored during phase calculation. It is better that no value of phase be calculated than that a random one be obtained. After the phase calculation was performed, the resolution of small sized details in the deformation pattern (signal spatial resolution) was of the order of a few pixels.

3.4 Strain calculation from the displacement maps

Strain components are related to displacement components of a deformation by the following relations :

$$\varepsilon_x = \frac{\partial d_x}{\partial x} \tag{54}$$

$$\varepsilon_y = \frac{\partial d_y}{\partial y} \tag{55}$$

$$\gamma_{xy} = \frac{\partial d_x}{\partial y} + \frac{\partial d_y}{\partial x} \tag{56}$$

where : d_x and d_y are the displacement components along the two in-plane directions x and y; ε_x and ε_y are the longitudinal strains along the same directions and γ_{xy} the shear strain.

In order to obtain both in-plane components d_x, d_y of the displacement, the specimen was rotated by 90° without moving the optical elements.

The displacement maps were imported in a commercial spreadsheet as arrays of numbers. This was accomplished through the use of a digitizing tablet.

The procedure for calculating spatial gradients of a deformation is always a delicate one, because in the differentiation process possible errors are amplified, as opposed to an integration process. Two different ways of obtaining strains were examined:

1) The finite-difference method (e.g. Hornbeck 1975), which evaluates point by point the derivative of the displacement plot using finite intervals of width h. These derivatives are accurate to within an error of the order of h. More terms in the Taylor series expansion can be taken in order to reduce this error (e.g. Herrera Franco 1985).

2) The least-square fitting method, which consists in fitting the displacement map with a 4th or 5th order least-square polynomial and then differentiating the polynomial along the in-plane directions. The displacement maps obtained with a phase-calculation algorithm are often affected by noise. Therefore a smoothing procedure such as the use of a least-square polynomial is often used to reduce noise levels (Vrooman and Maas 1991, Jia and Shah 1994). Moreover, this method is quick and gives a continuous plot of the strain values.

The latter method was used in this work. Since high spatial gradients of strains were expected near the hole, the displacement maps were fitted "piecewise". Different polynomials were used where the displacement maps presented marked variations in slope. Also, preliminary tests showed that for our kind of strain spatial gradients, the difference in resulting strain values between the two mentioned methods was within 5%.

3.4.1 Verification of the accuracy of the method: the cantilever beam experiment

In order to verify the accuracy of the described technique for strain analysis, a simple cantilever beam experiment was performed and results from electrical resistance strain gages were compared to the ones obtained with DSPI. A rectangular cross-section cantilever beam of a photoelastic material (length=6.5", width=0.75", thickness=0.5") was subjected to a load P≈0.5 lb. The specimen setup is shown in Figure 16. The Young's Modulus of the material was unknown; knowledge of it was unnecessary for the purposes of this experiment. Two strain gages of type EA-13-240LZ-120 by Measurements Group were installed in the upper and lower side of the beam. The two gages were taken from the same lot. Their properties were: R=120.0±0.3%, Gage Factor at 24°C=2.110±0.5%, K_t at 24°C=(0.2±0.2)%, Lot number R-A48AF154.

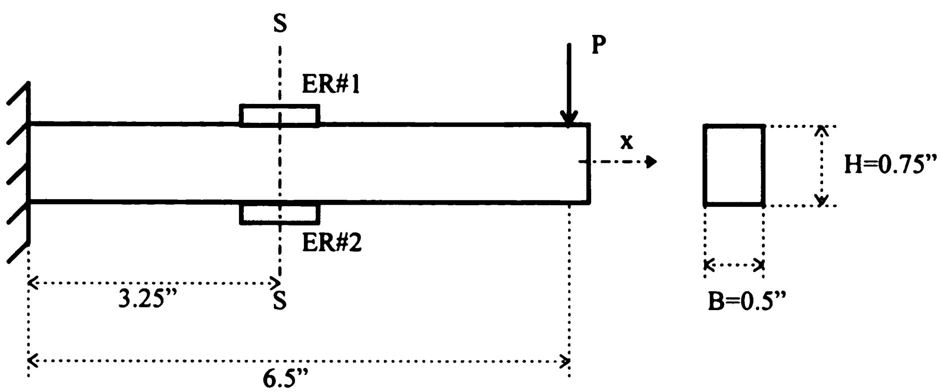

Figure 16. *Setup for the cantilever beam experiment.*

Before performing the test, the specimen was manually cycled in order to eliminate possible residual stresses and hysteresis.

The strain gages were connected to a P-3500 strain indicator, in a 1/4 bridge configuration. The two readings from the gages were taken for eight loading cycles. Zero readings were observed when load was removed, except for the first loading cycle which was therefore considered a "training" one. The gages were self-compensated (STC) for 2024-T4 Aluminum. Effects of thermal apparent strains were neglected because the tests were quick and no appreciable variation of temperature was observed during the measurements. The results showed an average value of 48μm/m and a standard deviation of 2μm/m for the upper gage (ER#1) and an average value of -38μm/m and a standard deviation of 2μm/m for the lower gage (ER#2).

The two different values of the indicated strains for upper and lower gages were at first unexpected. For a homogeneous beam, the two readings should have been equal and opposite. To be sure that this was not a systematic error due to the gages, some measurements were taken with the beam rotated by 180° about its longitudinal axis so that upper and lower gages resulted interchanged. Also in this configuration the results for the gage in tension and the one in compression were different, the latter showing always the lower absolute value of strain. It was concluded that the material tested had two different Young's moduli in compression and in tension. This is not unusual in plastic materials. In a case of a beam subjected to "pure bending", when the bending moment is constant in each section of the beam and no shear forces are present, the usual assumption that the sections remain "flat" after deformation implies that the strains are linear along a vertical direction (e.g. Shames 1964). When different moduli for traction and compression are present, in order to maintain equilibrium the stresses along a vertical direction have to be linear but with two different slopes for the part of the beam in tension and the part in compression. What happens in this case is therefore a "shift" of the neutral axis, as shown in Figure 17.

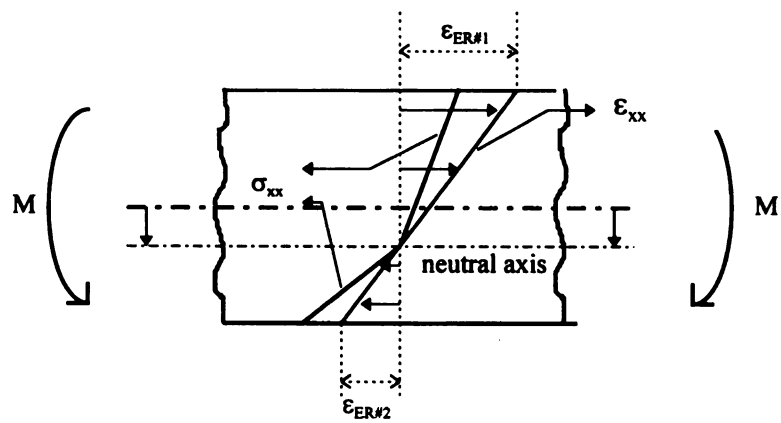

Figure 17. *Strain and stress distributions along a vertical section for a beam in pure bending with two different Young's moduli in tension and compression.*

It should be noticed that our configuration was not a case of pure bending (see Figure 16). In our case the bending moment was not constant along the length of the beam. With reasonable approximation, the condition of linear strain distribution can be assumed in cases like this where the applied loads are small.

An area of 0.75×0.75 in^2 of the beam was then analyzed with the in-plane phase-stepped DSPI technique. The same load as in the strain gage test was applied. The phase fringes obtained are shown in Figure 18.

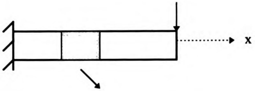

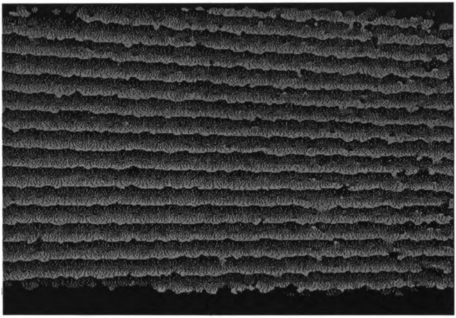

Figure 18. *Phase fringes obtained in the cantilever beam experiment.*

Note that the fringes in Figure 18 are not horizontal; rather they tend to converge towards the beam mid-plane as expected for a cantilever bending load condition. The slope of the fringes is opposite in the upper and lower part of the beam, showing that the upper part is in tension (positive ε_{xx}) whereas the lower part is in compression (negative ε_{xx}). Also, it can be noted that the slope of the fringes in the upper part is larger (in absolute value) than the slope of the fringes in the lower part. This means that the strains ε_{xx} in the part in tension are larger than those in the part in compression, at the same distance form the beam mid-plane. This observation confirmed the strain gage readings.

The strains were then calculated along the vertical section S-S (see Figure 16) as explained in Section 3.4, and the results are presented in Figure 19.

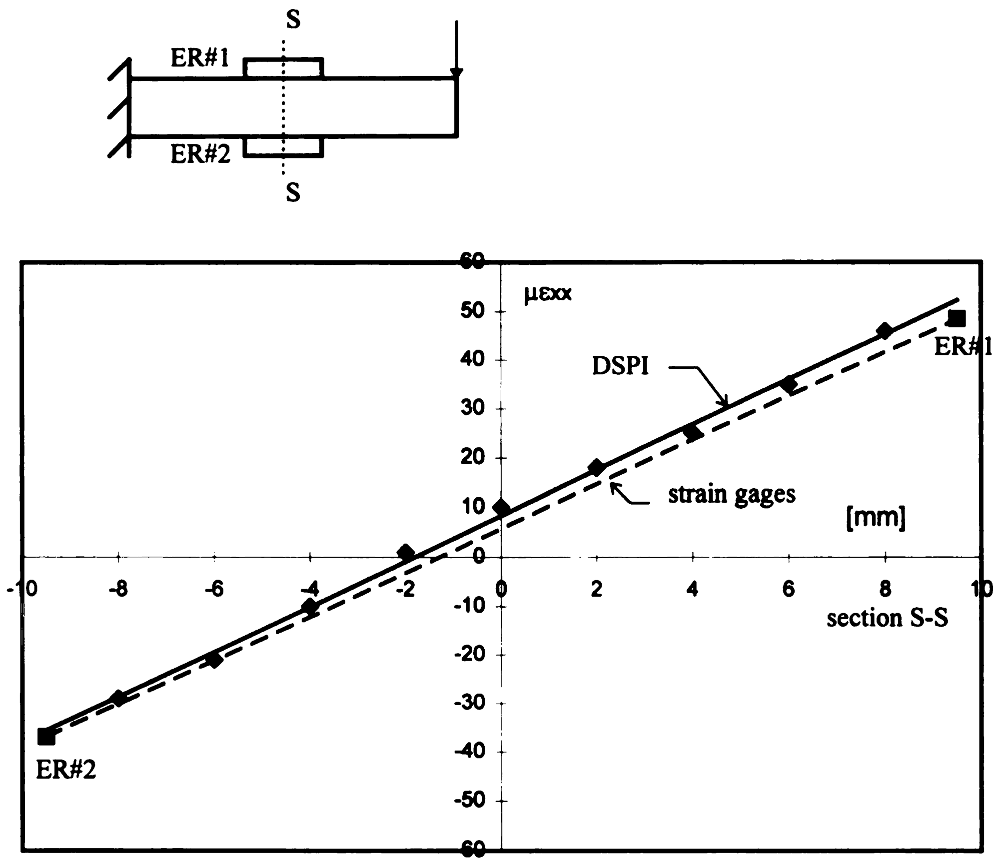

Figure 19. *Plots of strain ε_{xx} obtained with 1) DSPI and 2) strain gages, along section S-S of the cantilever beam.*

The distribution of strains obtained with DSPI along this vertical section was very close to linear, as expected. In Figure 19 the experimental points from DSPI are fitted with a least-square straight line. The outputs from the two strain gages are also connected with a straight line. The agreement between DSPI and strain gage results is shown to be to within 7%. These results established confidence about the accuracy of this method for strain measurements by phase-stepped DSPI.

CHAPTER IV

STUDY OF A SINGLE PIN-LOADED HOLE IN FIBER-REINFORCED PLASTIC

4.1 Introduction

In most composite mechanical structures, joints are the weakest elements. Among the mechanical fasteners, pins are widely used for simplicity of installation and reliability. The mechanical behavior of pin-loaded joints in composite materials is complicated by a number of factors such as fiber orientation, lay-up, friction, etc. More study is needed in this area to have a full understanding of this subject. DSPI is a quick and accurate technique for experimental mechanics and has been used for this purpose in the present work.

Strain and stress distributions are determined in critical locations near the hole in a pin-loaded joint of a fiber-glass reinforced epoxy laminate for a case of static tensile load. In this chapter a case of *perfect fit* (*"push-fit"*) between pin and hole is examined. The pin has nominally the same diameter as the hole.

Stress concentration factors are determined and compared with results from similar studies present in literature.

4.2 The specimen: geometry and mechanical properties

The material studied in this research was a glass-reinforced-epoxy $[0°/90°]_S$ laminate (R1500/1581, 13 plies, 0.14" thick) supplied by CIBA-GEIGY, Composite Material

Department, 10910 Talbert Avenue, Fountain Valley, California 92708.

The dimensions of the test coupon had to be chosen very carefully, because many studies have proved that geometric factors influence failure modes and elastic behavior of the specimen (see e.g. review paper by Godwin and Matthews 1980). Two geometrical factors were determinant and they are shown in Figure 20:

1) The ratio e/d between the distance "e" between hole center and free end perpendicular to the loading axis and the diameter "d" of the hole. The effect of end distance was investigated by Collings (1977) and it was determined that a minimum ratio e/d=3 was necessary to develop full bearing strength and to avoid end effects.

2) The ratio w/d between width of the specimen and diameter of the hole. Collings (1977) also determined that a minimum w/d=8 was required to have full bearing strength.

Our specimen had e/d=4 and w/d=8. It was cut in a previous research work (Herrera Franco 1985). The drilling of the through-the-thickness hole was carried out using two steel templates to avoid delamination. The pins used to load the specimen were stainless steel cylindrical pins 2" long. They were considered "perfectly rigid" throughout the work.

The laminate was constituted of 13 unidirectional plies. Each ply (lamina) could be considered orthotropic with two in-plane directions of material symmetry. Also the whole laminate could be considered "macroscopically" orthotropic: in fact, being a "cross-ply" laminate (0° and 90° fiber orientations), it had three mutually orthogonal planes of material symmetry. Therefore two principal in-plane material axes were present in the specimen and they are represented by axes "1" and "2" in Figure 20. These axes were also aligned with the natural axes of the specimen "x" and "y". For this reason, from now on it will be referred indifferently to reference system (1,2) or (x,y).

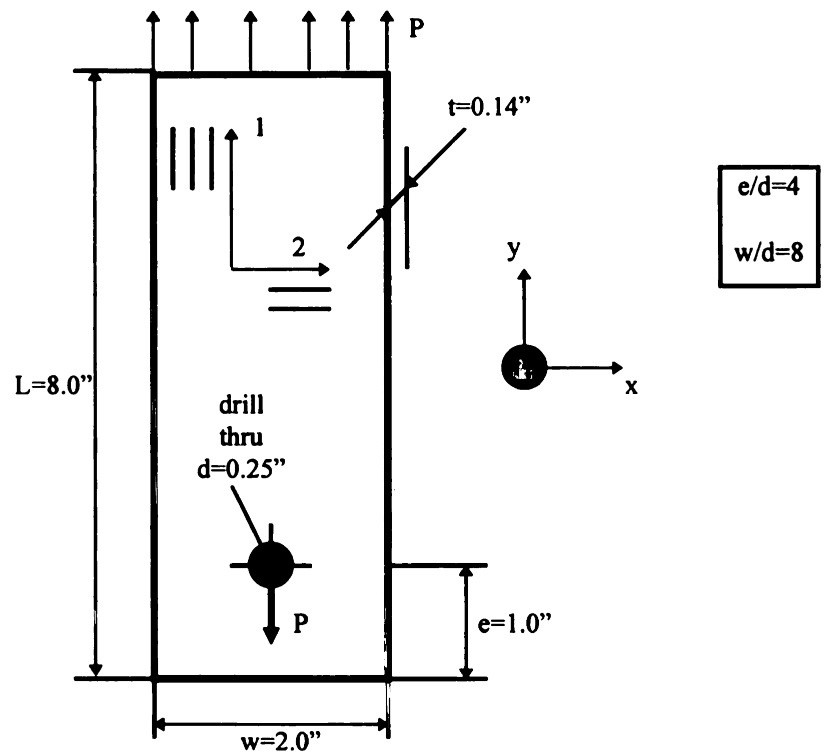

Figure 20. *Specimen used for the test: dimensions and loading condition.*

Because all the laminae were positioned symmetrically with respect to the laminate mid-plane, the specimen was a "symmetrical" laminate. The laminate was also "balanced", meaning that it contained an equal number of laminae at $+\theta$ degrees and $-\theta$ degrees fiber orientation with respect to its longitudinal axis. In this special case of a "symmetrical" and "balanced" laminate, there is no coupling between extensional and shear behavior and between extensional and curvature behavior; that is, extension forces will produce only extensions and bending moments will produce only curvatures.

The mechanical behavior of this specimen can be described by four independent "engineering" (also called "macroscopic" or "effective") constants (e.g. Whitney, Daniel and Pipes 1982), namely:

E_1, Young's modulus in direction 1; $E_1 = \sigma_x^o / \varepsilon_x^o$ when $\sigma_y^o, \tau_{xy}^o = 0$

E_2, Young's modulus in direction 2; $E_2 = \sigma_y^o / \varepsilon_y^o$ when $\sigma_x^o, \tau_{xy}^o = 0$

G_{12}, shear modulus in plane 1-2; $G_{12} = \tau_{xy}^o / \gamma_{xy}^o$ when $\sigma_x^o, \sigma_y^o = 0$

ν_{12}, Poisson's ratio for transverse strain in direction 2 and stress applied in direction 1,

$\nu_{12} = -\varepsilon_y^o / \varepsilon_x^o$ when $\sigma_y^o, \tau_{xy}^o = 0$.

where σ_x^o, σ_y^o , and τ_{xy}^o are the far-field applied stresses and ε_x^o, ε_y^o , and γ_{xy}^o are the longitudinal and shear mid-plane strains of the laminate along the (x,y) directions.

Therefore, the whole laminate could be macroscopically considered as an homogeneous and orthotropic lamina characterized by the "effective" mechanical properties mentioned above.

These properties were determined experimentally in the previous work by Herrera Franco (1985) and were found to be:

$E_1 = 3.188\times10^6$ psi (21.9804 GPa)

$E_2 = 3.0824\times10^6$ psi (21.2523 Gpa) (57)

$\nu_{12} = 0.11$

Looking at the two Young's moduli, it appears that the degree of anisotropy of the specimen is very low. Ideally, in a "cross-ply" laminate with the same number of plies at 0° and 90° orientation, it is $E_1 = E_2$. Because our specimen was constituted by an odd number of plies (13), it is believed that the ply corresponding to the laminate mid-plane was at 0° orientation, giving the specimen a slightly larger stiffness in that direction. The laminate under investigation could be reasonably considered "quasi-isotropic".

The shear modulus was unknown. An "engineering" shear modulus can be determined using the known relation for isotropic materials $G=E/2(1+\nu)$ with an average of E_1 and E_2:

$$G_{12} = \frac{avr(E_1, E_2)}{2(1+\nu_{12})} = 1.41\times10^6 \text{ psi } \ (9.72 \text{ GPa}) \tag{58}$$

Whitney *et al.* (1982) proposed an expression for G_{12} analogous to equation (58) for a $[\pm45°]_S$ laminate.

The second in-plane Poisson's ratio is determined by the known relation for orthotropic materials $\nu_{21}=\nu_{12}(E_2/E_1)$, giving in our case $\nu_{21}\approx\nu_{12}=0.11$.

For a generalized plane stress condition, the stress-strain relations (generalized Hooke's law) for an homogeneous and orthotropic laminate along the 1-2 directions can be expressed as (Lekhnitskii 1968):

$$\left|\begin{aligned}
&\sigma_1 = \frac{E_1}{1-\nu_{12}\nu_{21}}\varepsilon_1 + \frac{\nu_{12}E_2}{1-\nu_{12}\nu_{21}}\varepsilon_2 \\
&\sigma_2 = \frac{\nu_{12}E_2}{1-\nu_{12}\nu_{21}}\varepsilon_1 + \frac{E_2}{1-\nu_{12}\nu_{21}}\varepsilon_2 \\
&\tau_{12} = G_{12}\gamma_{12}
\end{aligned}\right. \tag{59}$$

These equations relate the average values of stress and strain components with respect to the thickness of the laminate, using the "effective" elastic constants for the laminate as a whole.

4.3 Experimental procedure

The specimen was loaded in tension using a stainless steel loading frame equipped with a hydraulic pump by Scott Engineering Sciences Corporation, as illustrated in Figure 21.

The loading frame was especially built to be very stiff. This was necessary in order to avoid any rigid body rotation of the specimen during the tests. Out-of-plane rotations didn't affect the measurements because the method was not sensitive to out-of-plane displacements. In-plane rigid body rotations, on the other hand, had a large influence on the calculation of the shear strain (which involves the crossed derivatives of the displacements) and therefore had to be minimized. The specimen was mounted in the loading frame using grips especially designed to allow rotations, thus avoiding any end effects.

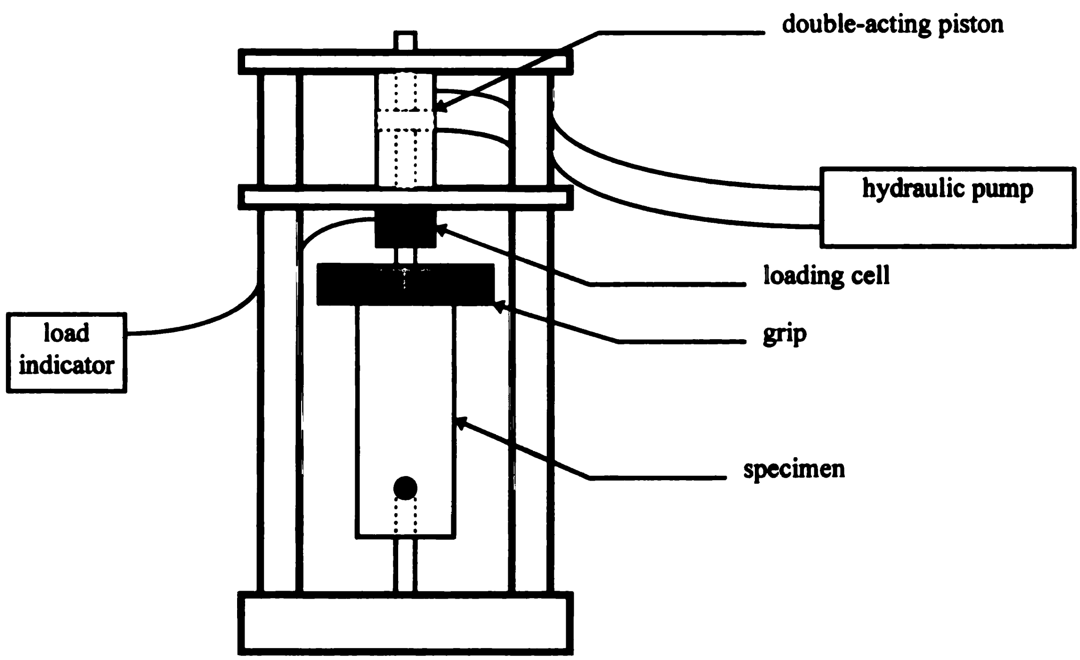

Figure 21. *Schematic of specimen and loading apparatus.*

Before taking the measurements the coupon was preloaded with about 10 lb so that it would self-align along the loading direction: this precaution reduced the chance of in-plane rigid body rotations during measurements. The applied load was measured using a loading cell by Photoelastic Division, Measurements Group, which was connected to a P-3500 strain indicator also by Measurements Group. The load values directly in pounds appeared in the strain indicator display. The net applied load was P=27 lb. This load provided a nominal far-field tensile stress $\sigma_y \approx 96.4$ psi. This small load was applied in order to avoid any plastic deformation in the specimen. The absence of plastic deformation was confirmed by the disappearance of the real-time correlation fringes when load was removed.

The procedure followed to determine the elastic behavior of the laminate near the pin-loaded hole was:

a) Measurement of displacements d_x and d_y using DSPI. The entire load frame with the specimen was rotated by 90° to measure both in-plane components.

b) Calculation of in-plane strain components ε_x, ε_y and γ_{xy} from equations (54)-(56).

c) Calculation of in-plane stress components σ_x, σ_y and τ_{xy} from equation (59), using the elastic properties of the laminate given in (57) and (58): determination of stress distribution near the hole and stress concentration factors (SCF's).

The final step of the analysis was the determination of the stress concentration factors (SCF's). Different ways of expressing the SCF's for mechanically fastened joints have appeared in the literature. In this work the maximum stresses at the critical locations of the specimen were related to the following "nominal "or "reference" stresses:

Far-field tensile stress $$\sigma_N = \frac{P}{w \times t} \tag{60}$$

Net tensile stress through the hole $$\sigma_{net} = \frac{P}{(w-d) \times t} \tag{61}$$

Average bearing stress $$\sigma_b = \frac{P}{d \times t} \tag{62}$$

where w, t, d and P are shown in Figure 20.

The DSPI technique measures displacements on the outside surface of the specimen. Therefore the strains calculated in step b) refer to the outside ply of the laminate. With a reasonable degree of approximation these strains can be referred to as average values for the laminate as a whole, and the stresses and SCF's calculated in step c) can also be considered average or "engineering" values referring to the whole specimen. This is considered reasonable also because this laminate is "symmetrical" with respect to its mid-plane; therefore, no curvature effects are present under tensile applied load.

For both isotropic and composite materials, there are three main failure modes in mechanically fastened joints (Matthews 1987): ligament tension, bearing and shear-out. These modes of failure are caused respectively by tensile normal stresses, compressive normal stresses and shear stresses. Figure 22 shows the location of these three types of failure.

The failure mechanisms of composites depend upon many factors such as fiber type, orientation, matrix, etc. In this work strains and stresses are determined along the critical locations shown in Figure 22. Some other locations near the loaded hole are also considered. All the analyses are carried out in the elastic range of the material.

Before testing the composite specimen, a preliminary experiment was performed with an isotropic specimen to check visibility and appearance of the DSPI correlation fringes. In this test no quantitative analyses were performed.

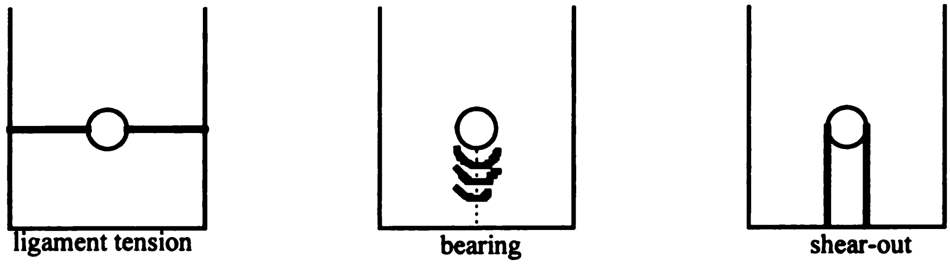

Figure 22. *Location of main failure modes in mechanically fastened joints.*

4.4 Experimental results and discussion

Figures 23 and 24 show the phase fringes obtained with DSPI for the component d_y of the displacement parallel to the direction of the load for the isotropic and the composite specimen respectively. Each fringe represents a displacement $d_y \approx 0.67 \mu m$. By following the evolution of the fringes in real time while increasing the load, it was determined that the fringe order increased going from the center of the hole towards the lower portion of the specimen and from the center of the hole towards the upper portion of the specimen. This was an indication of positive normal strains ε_y in the direction of the load in the upper part of the specimen and negative normal strains ε_y in the direction of the load in the lower part (bearing region). A high number of fringes per unit of length in the bearing/shear-out region indicates (1) large negative normal strains ε_y and (2) large shear strains γ_{xy}. Fringes almost perpendicular to the direction of the load in the upper region of the specimen indicate shear strains γ_{xy} nearly equal to zero.

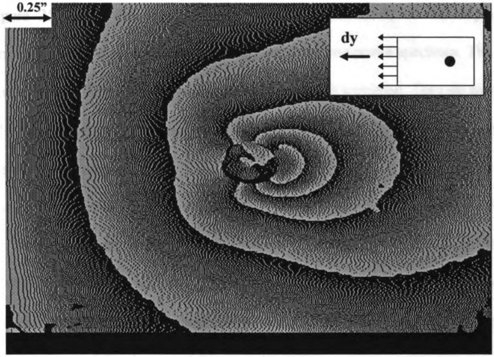

Figure 23. *DSPI phase fringes for displacement d_y parallel to the direction of load - Isotropic specimen.*

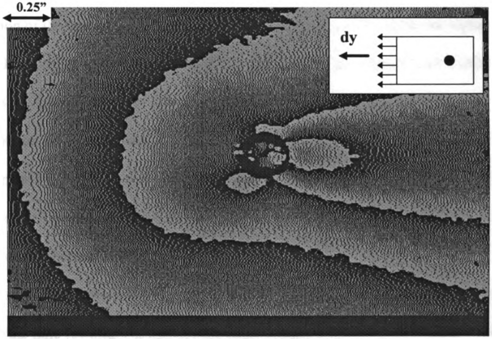

Figure 24. *DSPI phase fringes for displacement d_y parallel to the direction of load - Composite specimen.*

Figure 25 shows the phase fringes for the component d_x of the displacement perpendicular to the direction of the applied load in the composite specimen. The fringes in Figure 25 were obtained by applying a large load to the specimen. They do not refer to the 27 lb load experiment. The large load was applied to obtain an appreciable number of fringes for the d_x component.

For the strain/stress calculation, a load equal to 27 lb was applied, as explained earlier. Even if this load produced only one or two correlation fringes in the specimen, the phase-stepping technique was able to give results with a resolution of a few pixels: the biggest advantage of the use of phase measurement techniques such as phase-stepping is that there is no need for the use of fringe multiplication techniques even in cases where only few fringes are observed.

Figure 25 can be used for qualitative analysis. Fringes almost perpendicular to the direction of the applied load indicate high shear strains γ_{xy} in the shear-out region. On the other hand, fringes almost parallel to the direction of the applied load indicate shear strains γ_{xy} nearly equal to zero in the region above the hole. The non-symmetrical distribution of fringes with respect to the longitudinal axis of symmetry "y" of the specimen is probably due to variations of mechanical properties over the specimen itself. A possible cause of this is a variation in fiber volume fraction in the plies and/or a variation in fiber orientation.

Plots of strains were obtained for three regions around the loaded hole: (1) the region below the hole (bearing region); (2) the region above the hole; (3) the net-section region (ligament region).

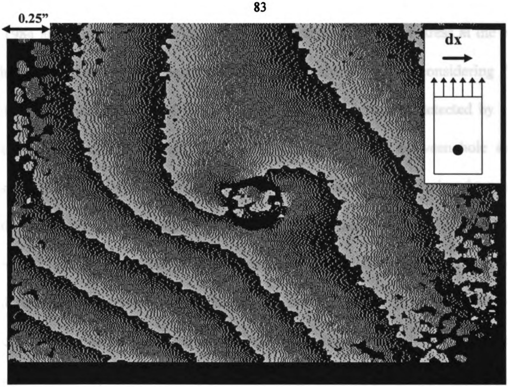

Figure 25. *DSPI phase fringes for displacement d_x perpendicular to the direction of the load- Composite specimen.*

Figure 26 shows strains ε_y parallel to the direction of the load along the vertical diameter of the hole in the bearing region.

The high value of the bearing strain near the hole vanishes at a distance from the edge of the hole approximately equal to the radius r of the hole. Since a monotonic decrease in bearing strain is expected from the hole to the free edge of the specimen, the slight increase in compressive strain observed at a distance from the edge of approximately 1.5 times the radius r of the hole is believed to be caused by nonhomogeneous distribution of mechanical properties of the specimen.

The maximum compressive strain is shown to be not at the edge of the hole, but at a certain distance from it. This effect was not reported by some authors (e.g. Pradhan and

Ray 1984 and De Jong 1977) who always found maximum bearing stress at the edge of the hole. These researchers used finite element analysis without considering friction effects. The behavior observed in the present work was, however, detected by Herrera Franco (1985) and it is probably due to the effect of friction between hole and pin. Eriksson (1986) and Hyer *et al.* (1987) proved independently that friction decreases the radial bearing stress at the edge of the hole. This is physically correct because frictional forces will transfer axial load through tangential stresses and, owing to equilibrium, the radial stress must decrease. They also proved that this effect is more marked on the vertical diameter of the hole than in any other diametrical locations around the edge of the hole. Moreover, the frictional forces at the edge of the hole on the vertical diameter give a positive bearing strain ε_y due to the Poisson effect ($\varepsilon_{bearing(1)}$ in Figure 27). The superimposition of the negative bearing strain due to the axial load ($\varepsilon_{bearing(2)}$ in Figure 27) and the positive strain due to friction produces a lower resultant negative bearing strain on the vertical diameter at the edge of the hole. This effect is illustrated in Figure 27.

Figure 28 shows strains ε_y along lines parallel to the axis of the load for the ligament area. The highest strain values are obtained along the line tangent to the hole. A decrease in strain by a factor of about 2 is observed at a distance from the hole equal to 0.5*r along the "x" axis, r being the radius of the hole. This is representative of the high spatial stress/strain gradient near the hole. Pradhan and Ray (1984) determined that the rate of decay of stresses along the axis through the pin perpendicular to the loading force is higher in orthotropic plates as compared to isotropic plates.

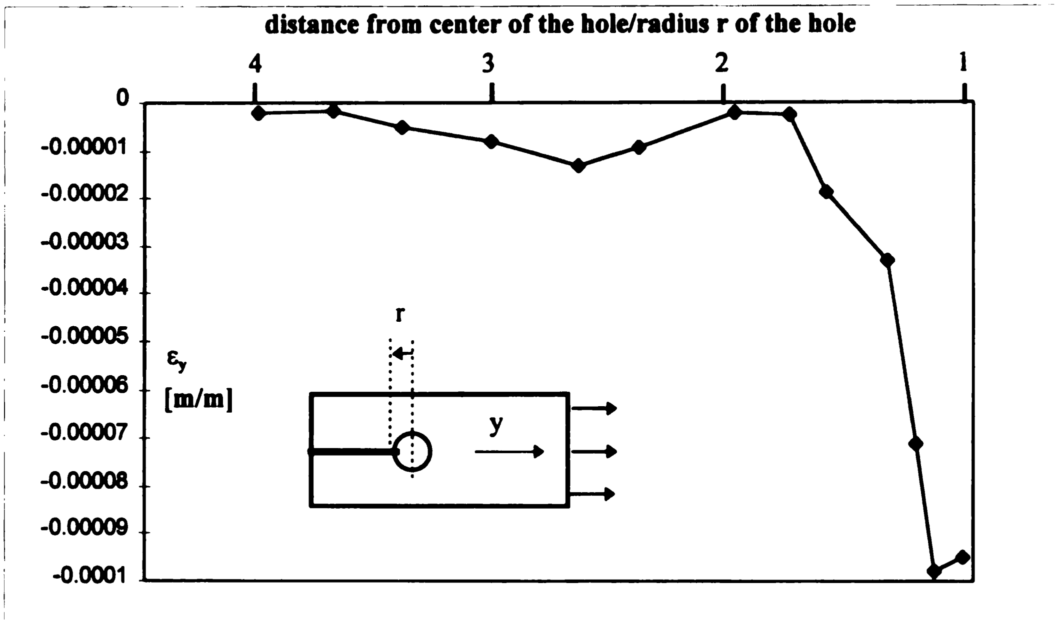

Figure 26. *Strains ε_y parallel to the direction of the load along vertical diameter in the bearing region.*

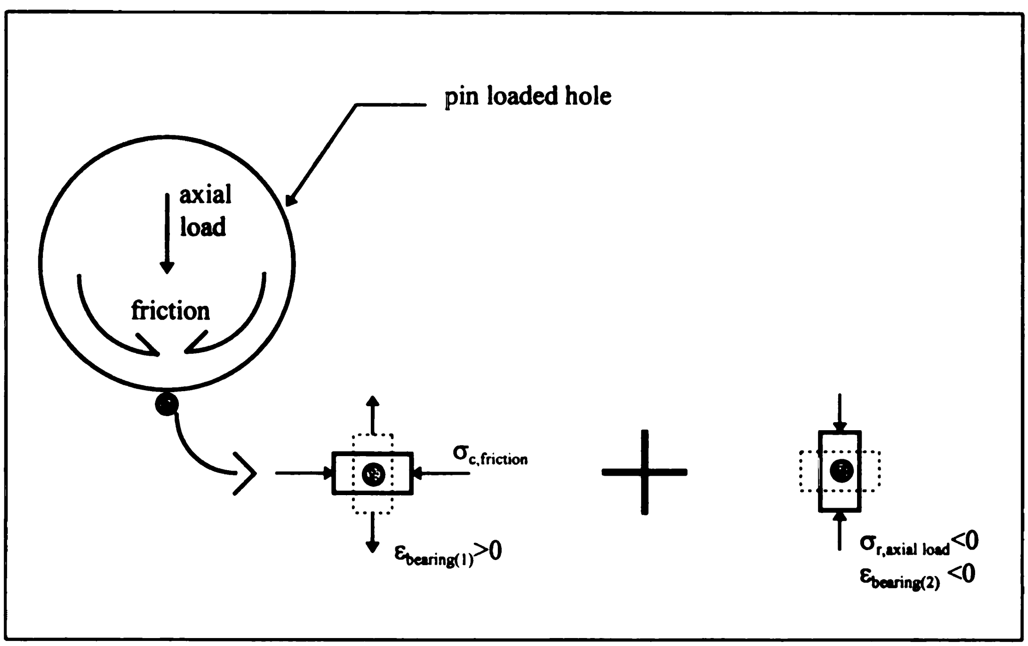

Figure 27. *Effect of friction on bearing strain.*

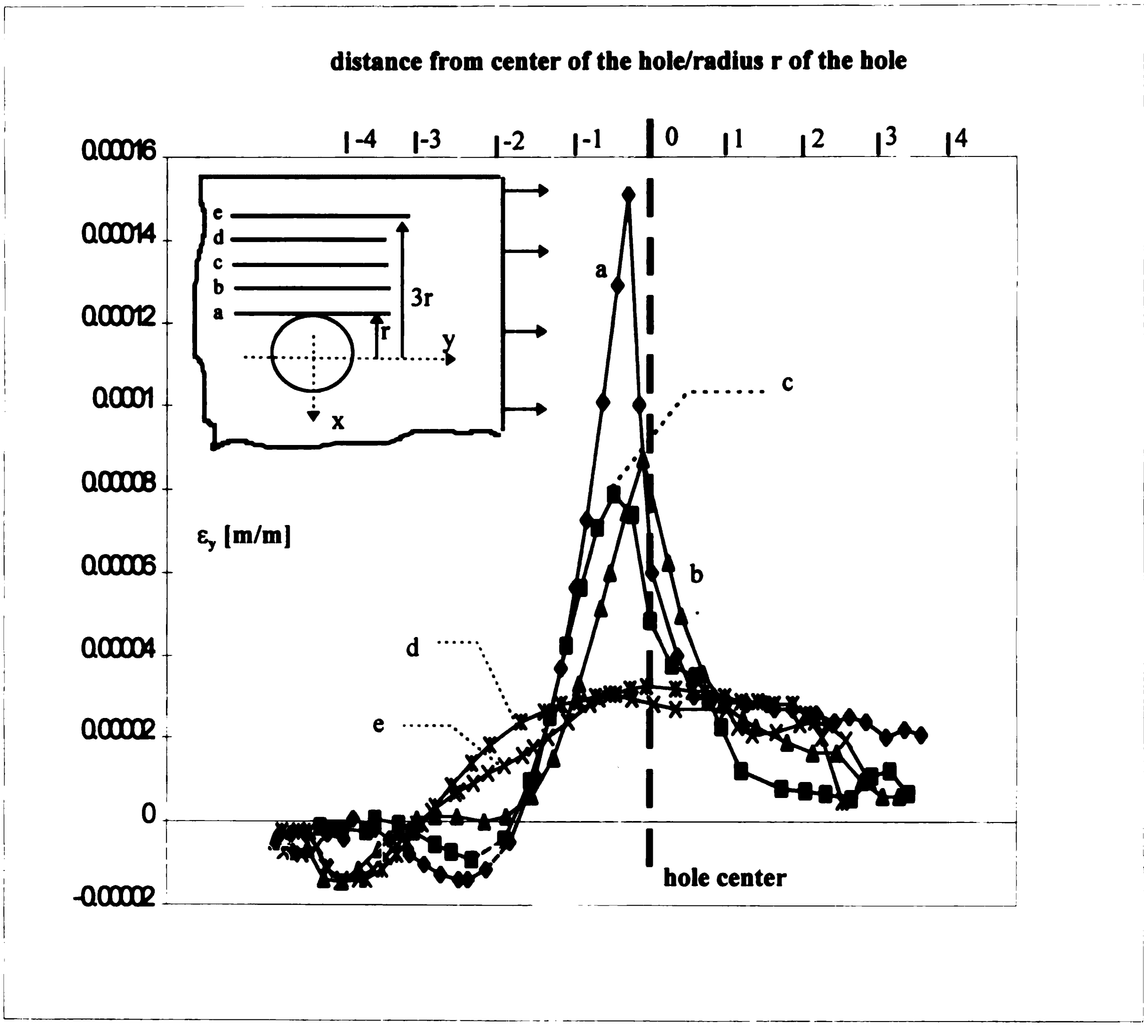

Figure 28. *Strain ε_y along lines parallel to the direction of the load located in the ligament area.*

Also in Figure 28, the high strain near the hole decreases to an approximately constant average value far from the hole. Above the hole the normal strain is positive (tensile area), and below the hole it is negative (compression area) owing to the bearing effect.

It is observed that the maximum value of the strain does not occur at the end of the horizontal diameter of the hole, i.e. in the minimum net area of the plate, but slightly below the hole. The same effect was observed by Herrera Franco (1985). Also Nisida and Saito (1966) showed that the maximum value of circumferential stress at the edge of the hole does not occur in the minimum net section but at an angle φ of about 85° from the vertical diameter below the hole. Frocht and Hill (1940) observed that the maximum stresses do not occur at the ends of the horizontal diameter when there is clearance between pin and hole. These two studies were on isotropic plates. Eriksson (1986) found that the maximum circumferential stress occurs at an angle φ of about 80° in a composite plate. Hyer *et al.* (1987) found this angle to range from 70° and 88° for different laminate lay-ups and attributed this to effects of friction, clearance and contact angle between pin and hole. De Jong (1977) found that the maximum normal stress in the direction of the applied load occurs at an angle φ of about 80°. Zhang and Ueng (1984) found the maximum circumferential stress angle to be about 75° for a [0°/45°] laminate and about 45° for a [90°/45°] laminate.

Figure 29 shows strains ε_x perpendicular to the direction of the load along parallel lines located above the hole. The highest transverse strain is shown to be along the vertical diameter of the hole. The strain becomes small away from the hole. The negative

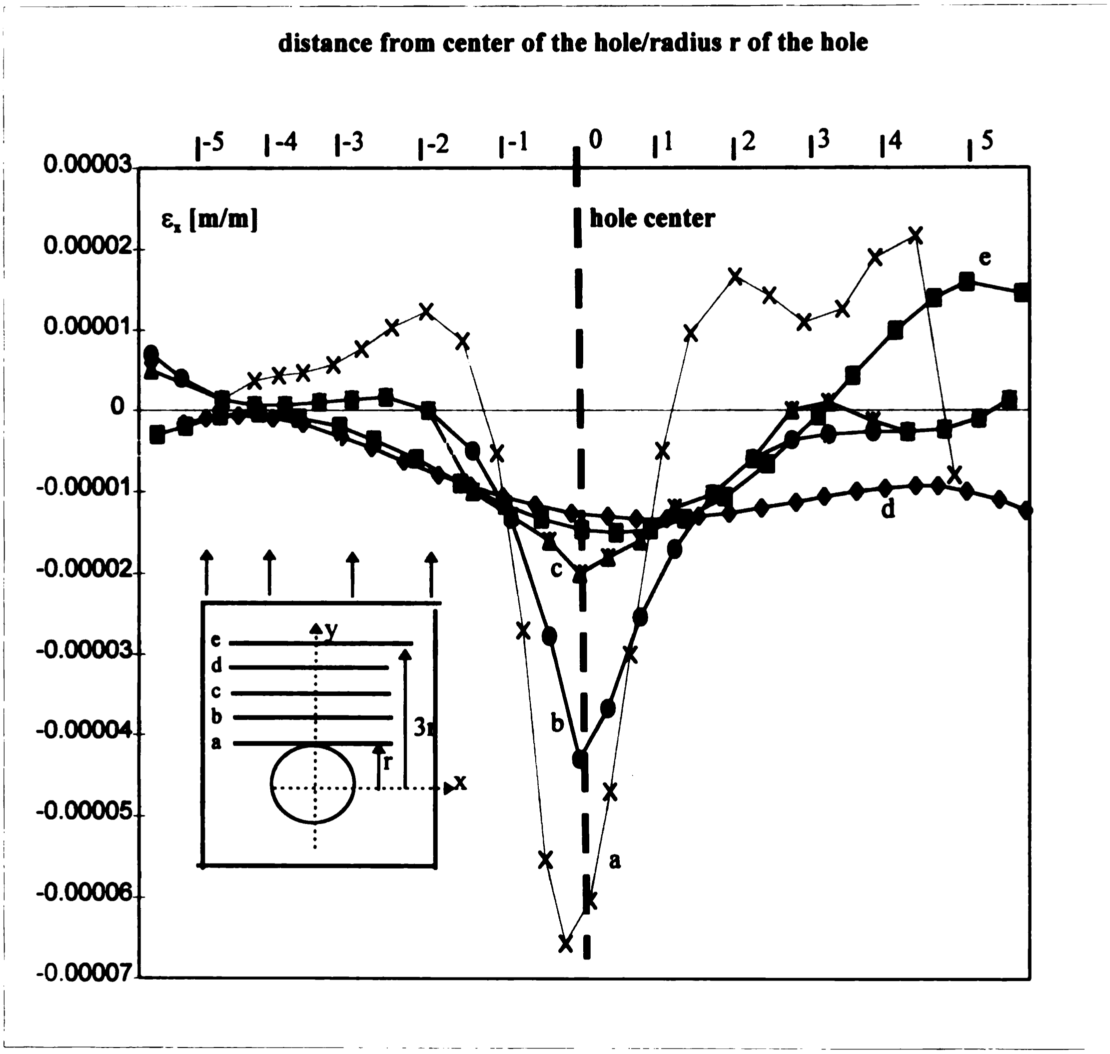

Figure 29. *Strain ε_x along lines perpendicular to the direction of the load located above the hole.*

sign of the strain on the vertical diameter of the hole under tensile applied load is caused by the Poisson effect. A compressive (negative) circumferential stress is present on the upper edge of the hole along its vertical diameter. This finding is consistent with results from several authors (e.g. De Jong 1977). Away from the hole, where the stress concentration is small, the strain ε_x assumes a constant average value. A slight asymmetry with respect to the specimen vertical axis is noticed in the plots of Figure 29: this can be attributed to variation in mechanical properties across the specimen.

Figure 30 shows strains ε_x perpendicular to the direction of the load along parallel lines located below the hole (bearing zone). The highest value of strain is observed along the vertical diameter of the hole. Its positive sign is due to the Poisson effect and the bearing load induced by the pin. The circumferential stress at the lower edge of the hole along its vertical diameter has a positive sign (tensile). This is confirmed by results obtained by other authors (e.g. De Jong 1977). The strain value diminishes away from the hole. The general behavior of these plots is similar to that found by Herrera Franco (1995) for the same material. The asymmetry with respect to the vertical axis of the specimen in the plots of Figure 30 can be again attributed to variation in mechanical properties of the specimen.

Figure 31 shows the shear strain γ_{xy} along a vertical tangent to the hole in the lower part of the specimen. This is the usual location of the shear-out failure mode. The value of γ_{xy} on the horizontal diameter of the hole ("x" axis) is shown to be different from zero. When no friction between pin and hole is present, the shear stress at the edge of the hole along its horizontal and vertical diameters is shown to be nearly zero by several

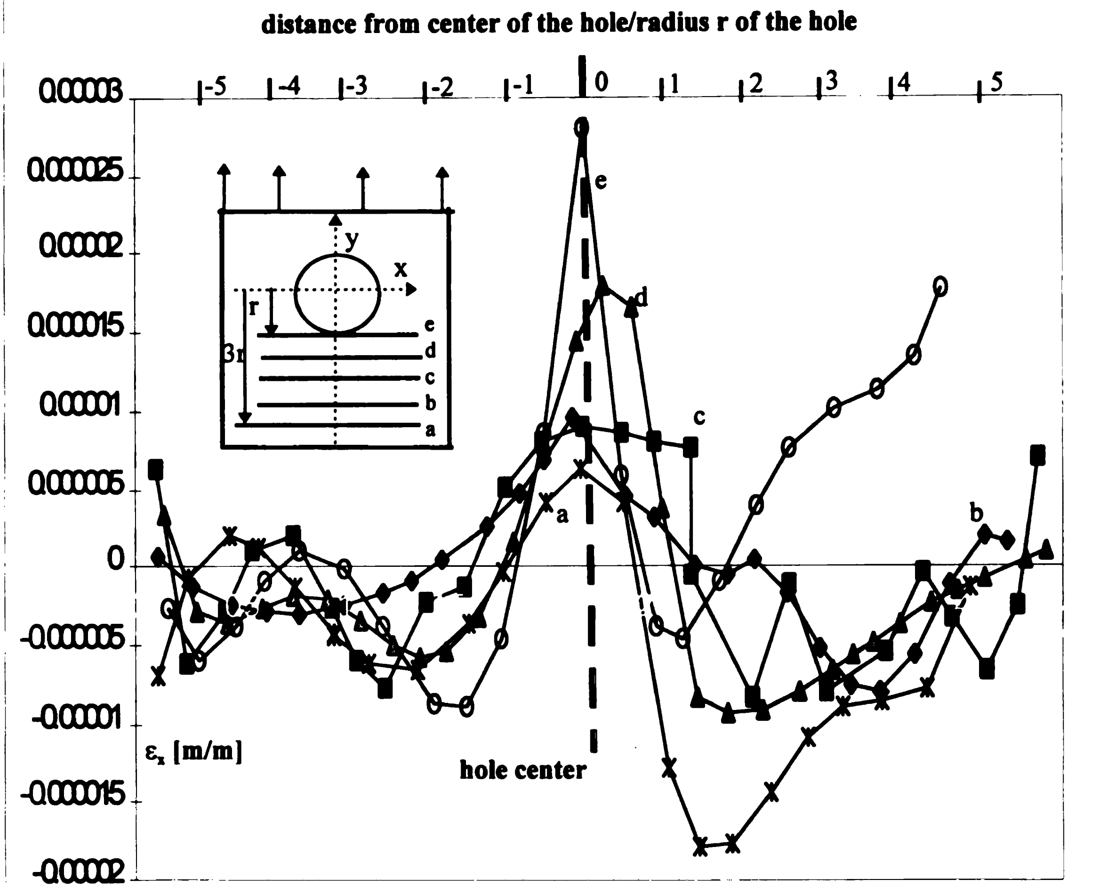

Figure 30. *Strain ε_x along lines perpendicular to the direction of the load located below the hole (bearing zone).*

investigators (e.g. Matthews *et al.* 1982, Pradhan and Ray 1984). The value different from zero of shear strain in the horizontal diameter on the edge of the hole in Figure 31 is due to friction, as showed by Zhang and Ueng (1984).

γ_{xy} is shown to be maximum at a distance equal to one radius r from the edge of the hole along the shear-out-direction. At points located far from the hole, the shear strain becomes smaller. This is qualitatively consistent with results from other authors; for a case of carbon fiber reinforced plastic (CFRP) unidirectional composite laminate, Pradhan and Ray (1984) showed that the maximum shear stress occurs in the shear-out area at an angle of about 60° from the horizontal diameter ("x" axis) of the hole. De Jong (1977) found this angle to be about 70° for the same laminate.

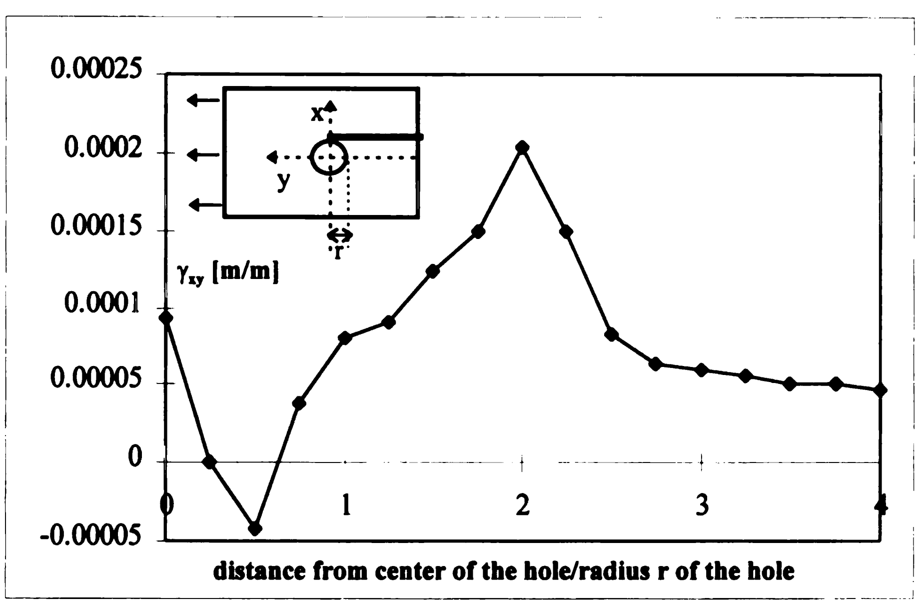

Figure 31. *Shear strain γ_{xy} along location of shear-out failure.*

Figure 32 shows qualitatively the locations of the maximum stresses found in the specimen, for the three possible failure modes: normal tensile stress σ_{ymax} in the ligament region, normal compressive stress σ_{ymin} in the bearing region and shear stress τ_{xymax} in the shear-out region.

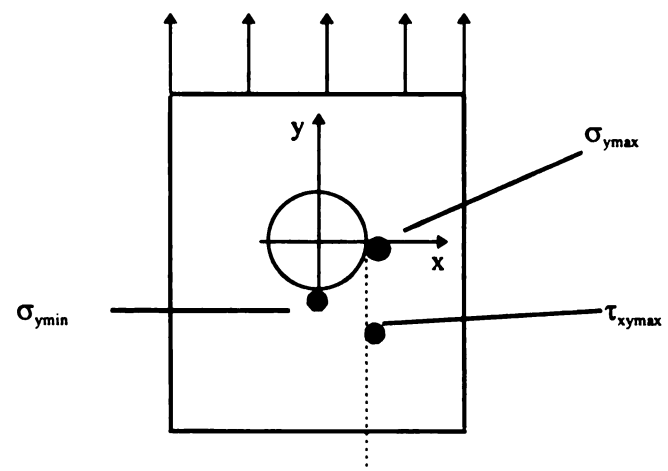

Figure 32. *Location of maximum stresses near the hole.*

Table 1 shows the values of stress concentration factors (SCF's) calculated for this case of perfectly fitted pin in the present research. Results from two other studies by De Jong (1977) and Matthews *et al.* (1982) are also presented for comparison. The reference stresses used to express the SCF's have been presented in Section 4.3 in equations (61) and (62).

Table 1. *Comparison of SCF's determined in the present work, by Matthews et al. (1982) and by De Jong (1977). FGRP=fiber glass reinforced plastic; CFRP=carbon fiber reinforced plastic.*

	Present analysis	**Matthews *et al.* (1982)**	**De Jong (1977)**	
Material tested	$[0°/90°]_S$ FGRP	$[0°/\pm45°/0°]_S$ CFRP	$[90_4°/\pm45°]_S$ CFRP	$[0°/\pm60°]_S$ elastically isotropic CFRP
Method used	Phase-Stepped DSPI	3-D FEM	Complex Functions	
$K_b^y = \dfrac{\sigma_{y\max}}{\sigma_b}$	0.63	1.79	1.2	0.8
$K_{net}^y = \dfrac{\sigma_{y\max}}{\sigma_{net}}$	4.38	5.37	4.95	4.89
$K_b^{xy} = \dfrac{\tau_{xy\max}}{\sigma_b}$	0.37	0.56	0.5	0.6

Table 1 shows that the SCF's found in the present analysis are all lower than the ones obtained by the other authors. This mismatch can be attributed to differences in mechanical properties of the materials tested, which highly affect the stress concentration factors. In the other two analyses mentioned, carbon-fiber reinforced plastic was tested and this material is generally stiffer than fiber-glass reinforced plastic which was used in this work (to give an idea, for a unidirectional lamina, tensile longitudinal modulus is 40 GPa for a 60% volume fraction E Glass/Epoxy, as opposed to 210 GPa for a 62% volume fraction High Modulus Carbon/Epoxy, according to Chawla (1987)). Rowland *et al.* (1982) pointed out that softer materials always exhibit lower stress concentration factors than stiffer ones, because they are more able to wrap around the pin and therefore to distribute the pressure more evenly over the edge of the hole. Pradhan and Ray (1984), using FEM, found that the maximum stress around the hole was high in the case of graphite/epoxy and boron/epoxy unidirectional laminae compared to the case of glass/epoxy.

As observed in Section 4.2, the laminate tested in this research can be considered quasi-isotropic, because the ratio E_1/E_2 is very close to 1. Indeed, our results are closer to those presented in the last column of Table 1, which refers to an elastically isotropic material, the larger mismatch being in the shear stress concentration factor.

CHAPTER V

STRESS CONCENTRATION RELIEF BY THE USE OF INTERFERENCE-FIT PINS

5.1 Introduction

Machine assemblies are often prestressed to eliminate stress gradients and to increase fatigue life.

Let us suppose that a strip with a bolted connection is subject to an axial cyclic pulsing load as shown in Figure 33.

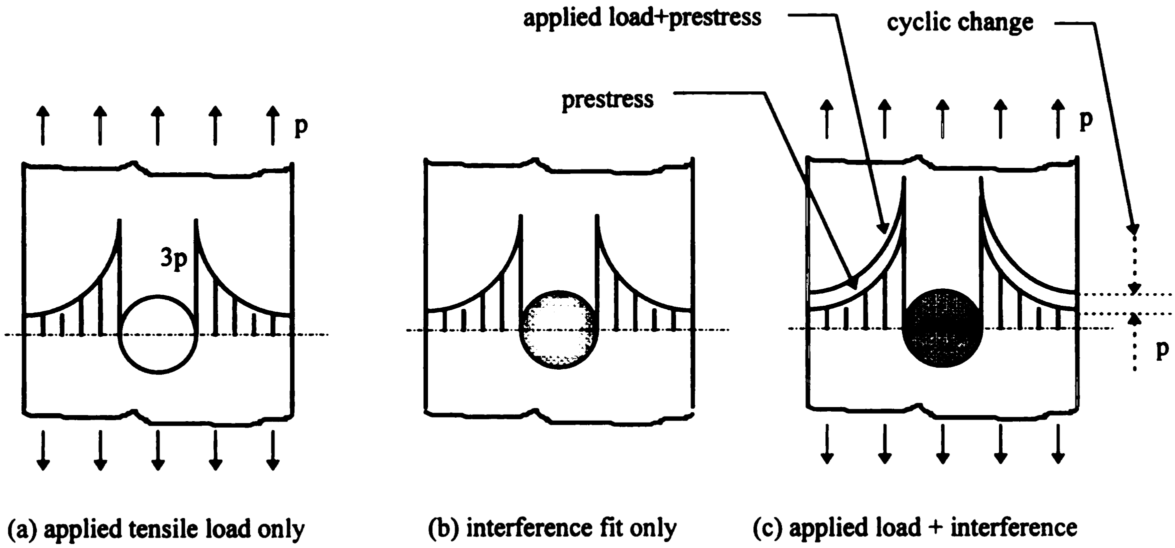

Figure 33. *Effect of the prestress due to an interference fit on the stress distribution near the hole for a case of isotropic strip subjected to axial pulsing load (from Regalbuto and Wheeler 1970).*

If no prestress due to interference between pin and hole is present, the axial stress at the edge of the hole will rise from zero to roughly 3 times the far field stress applied to the ends of the plate. When an interference fit exists between pin and hole, a state of initial biaxial stress is created near the hole. When the tensile load is applied, the resultant stress is not given by the simple addition of the two stress distributions caused by the interference and the applied load. What has been observed (Love 1963) is a profile obtained by adding the average tensile stress to the initial prestress distribution. Even if the average stress is increased, the *change* in stress level is now only p, as opposed to 3p for the case of no prestress. This *decrease in change* of stress causes an increase in fatigue life of the component, the fatigue life being influenced more by the alternating component of the stress than by its mean value.

In a case of a static load the effect of the prestress induced by an interference fit is to decrease the *change* in peak tensile or shear stress produced by the applied tension. This effect is illustrated in Figure 34, which refers to the study by Jessop *et al.* (1956) of an isotropic plate with hole subjected to static tensile load at the ends. Figure 34 shows the variation of maximum shear stress at the edge of the hole with the applied load, for the case of perfect fit and two cases of interference; the effect of interference is to decrease the *slope* of these lines.

For a plate loaded in tension through the pin, the beneficial effect of an interference fit between pin and hole is qualitatively the same as the case of a plate loaded at the ends (Jessop *et al.* 1956 and 1958). The effect of interference has been studied by some authors (see Section 1.3.3) for both isotropic and composite materials. Especially for the latter, a complete understanding of the problem is yet to be completed.

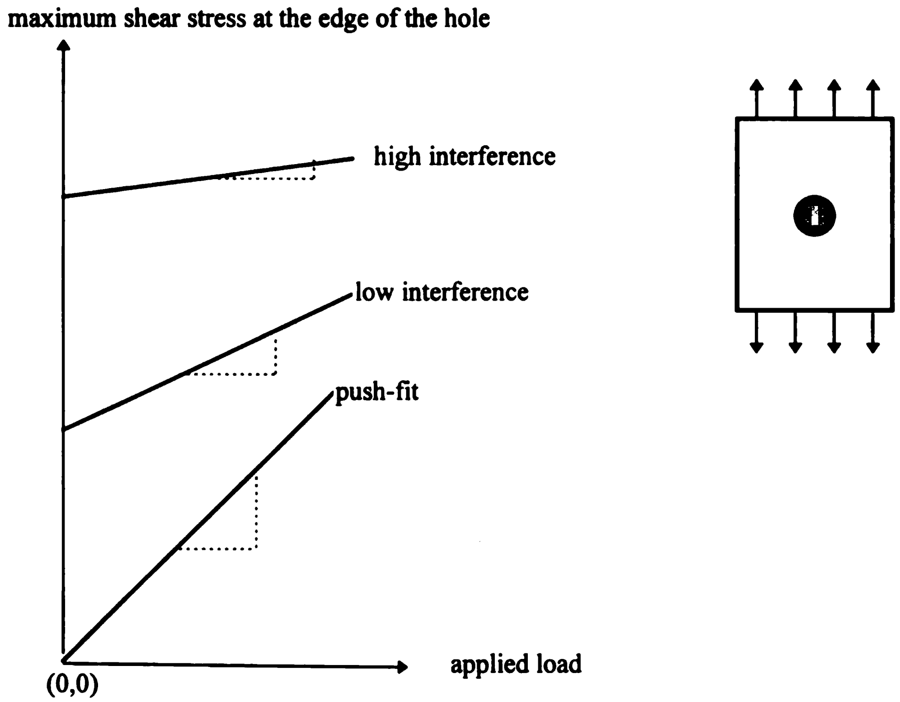

Figure 34. *Schematic of variation of maximum shear stress near the hole with applied static load, for perfect fit and two cases of interference fit (from Jessop et al. 1956).*

In this work two degrees of interference fit between pin and hole were investigated.

"Low" interference : $I = (d'-d)/d = 0.0002$

"High" interference : $I = (d'-d)/d = 0.0004$

where d' and d are the diameters of pin and hole respectively.

In order to obtain these values of interference, pins measured to an accuracy of 0.0001" were used. Before installation, the larger pin was cooled down with liquid nitrogen to cause a thermal contraction. The smaller pin was simply pushed into the hole manually. Particular care was used in this process in order to avoid delamination of the specimen.

The specimen tested was the same as the one used for the perfect-fit case (Capter IV). The axial loads used in these tests were P=27lb for the low interference test (far field stress σ_y=96.43psi) and P=34lb for the high interference test (far field stress σ_y=121.43psi).

The first concern was to be sure that these values of interference and the applied load would not cause plastic deformation in the specimen. The theoretical solution for pins with interference fit in a circular hole in an infinite isotropic plate is given by A.C. Stevenson. For a rigid pin of diameter (d+ε) inserted in a hole of diameter d in an infinite plate, the stresses at the hole boundary are given by

$$\sigma_{\theta\theta int} = -\sigma_{rrint} = 2G\varepsilon/d, \tag{63}$$

where G=shear modulus of the plate= $\dfrac{E}{2(1+\nu)}$

To a first approximation, as explained in Section 4.2, the laminate tested in this research can be considered quasi-isotropic with a shear modulus $G=1.41\times10^6$ psi. The values of the stresses at the edge of the hole due to interference are given by equation (63) which in our case yields:

"Low" interference: $\sigma_{\theta\theta int} = -\sigma_{rrint} \approx 560$ psi

"High" interference: $\sigma_{\theta\theta int} = -\sigma_{rrint} \approx 1{,}120$ psi

The highest nominal tensile stress in the net section due to the applied load was σ_{load}=140psi (case of high interference: applied load P=34 lb). Multiplying this value by the stress concentration factor K^{θ}_{net}=4.38 from Table 1 in Section 4.4, gives the maximum tangential stress at the edge of the hole caused by *only* the applied load $\sigma_{\theta\theta load}$=481psi. It has been mentioned (see Figure 33) that the resultant stress at the edge of the hole due to interference and applied tensile load is always *less* than the simple addition of the two stresses $\sigma_{\theta\theta int}$ and $\sigma_{\theta\theta load}$. The value $\sigma_{tot} = \sigma_{\theta\theta int} + \sigma_{\theta\theta load} = 1{,}120 + 481 = 1{,}601$psi constitutes therefore an excessive estimate of the actual resultant maximum stress in the plate.

The minimum tensile strength in a fiber glass reinforced epoxy unidirectional lamina is the strength in the direction perpendicular to the fibers. Chawla (1987) reports for this parameter a value of $\sigma_{yield} \approx 4{,}000$ psi for an E-glass reinforced epoxy. Since this value is much larger than the calculated σ_{tot}=1,601psi, we had a large margin of confidence that the material would never undergo plastic deformations during the tests. This was confirmed experimentally by the disappearance of the real-time correlation fringes upon removal of the load.

It is important to realize that in the present research the specimen *already prestressed* with an interference fit was tested with DSPI. The initial ("undeformed") state was therefore the prestressed state and the final ("deformed") state was the resultant state of prestress+applied-load-induced stress. The results obtained are therefore representative of the *change* in stress distribution due to the applied load. They do not represent the resultant, actual distribution of strain/stress in the specimen. It is the *diminution of this change* due to the applied load that is observed when an interference fit is used. Of course, in the case of perfect fit, the measured stress/strain distributions are the actual distributions in the specimen.

5.2 Experimental results and discussion

Plots of stress distributions in critical locations near the hole are obtained following the procedure explained in Section 4.3. The two cases of interference fit are compared to the case of perfect fit between the pin and the hole. For comparison, the stress values are normalized with the reference stresses illustrated in equations (60)-(62) in Section 4.3.

Figure 35 shows the distribution of the normal stress σ_y parallel to the direction of the load along the ligament area for the case of perfectly fitted pin and the two cases of interference fit. The values of the stress σ_y are normalized with the far field nominal stress $\sigma_N=P/(w\times t)$. In all three cases the stress assumes an almost constant value at a distance of about $1.5\times r$ from the edge of the hole, r being the radius of the hole. A marked decrease in stress concentration factors is observed for the cases of interference fit. This decrease is bigger for the case of high interference.

Figure 36 shows the distribution of the normal compressive stress σ_y parallel to the direction of the load in the bearing region for the case of perfectly fitted pin and the two cases of interference fit. The stresses are normalized with the bearing reference stress $\sigma_b=P/(d\times t)$. The bearing effect almost vanishes at a distance from the edge of the hole equal to $1\times r$, r being the radius of the hole, for the perfect fit and the low interference cases. For the case of high interference this distance is found to be about $2\times r$. The maximum stress concentration factor decreases when the level of interference is increased.

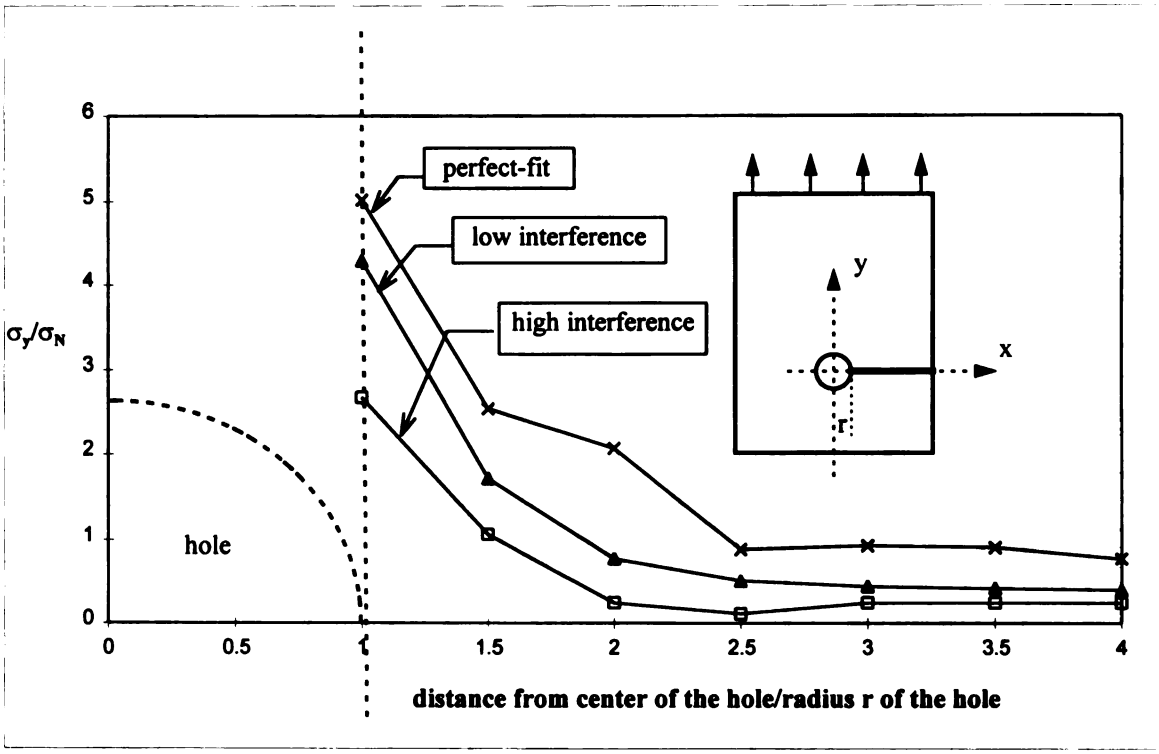

Figure 35. *Normal stress concentration factor* σ_y/σ_N *along the ligament area for (1) perfect fit, (2) low interference fit, (3) high interference fit.*

Figure 36 shows that the maximum stress never occurs at the edge of the hole, but rather occurs at a certain distance from it for all the three cases examined, the largest distance being for the high interference case (1×r). As discussed in Section 4.4 (Figures 26 and 27), this can be attributed to friction effects between the pin and the hole, which decrease the radial bearing stress at the edge of the hole (Hyer *et al.* 1987). This hypothesis is confirmed by the plots in Figure 36, where this behavior is more marked for the case of high interference fit, where larger friction forces than the other cases are present.

Also, it can be noted in Figure 36 that the stress value at the edge of the hole is smaller in the low interference case than it is in the high interference case. A similar behavior was observed by Jessop *et al.* (1958), in their studies on pin-loaded joints for isotropic materials. They concluded that there is an optimum value of interference, for a given applied load, at which the reduction of the stress in certain locations at the edge of the hole is maximum.

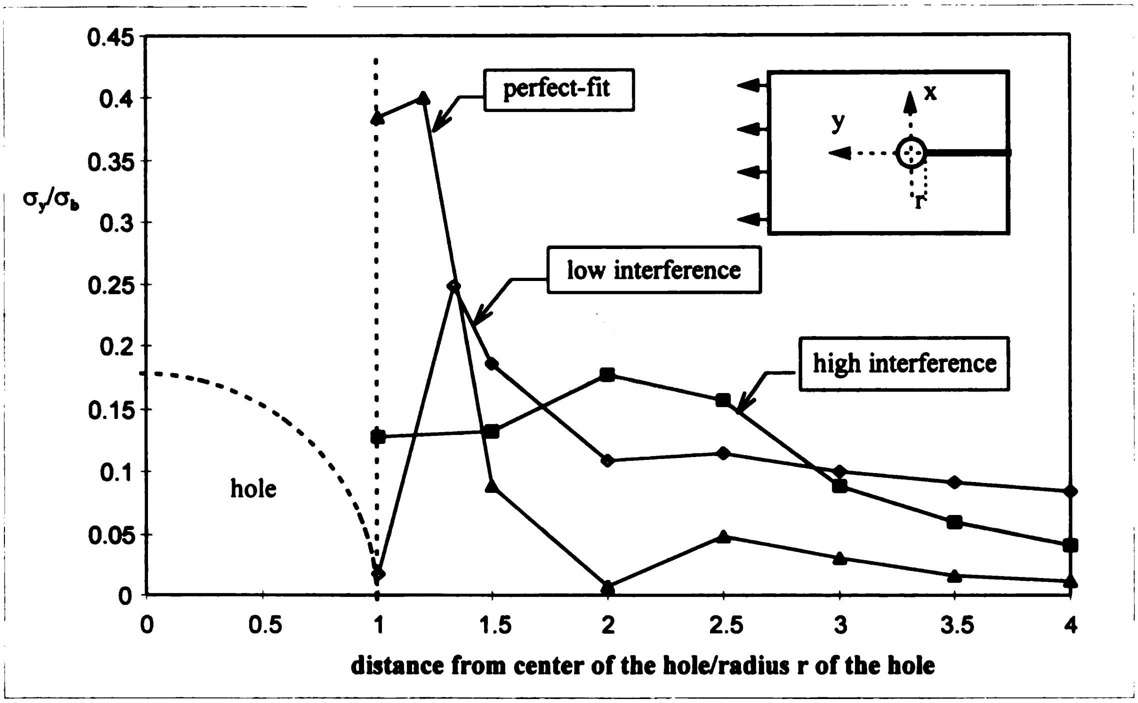

Figure 36. *Bearing stress concentration factor σ_y/σ_b along the bearing region for (1) perfect fit, (2) low interference fit, (3) high interference fit.*

Figure 37 shows the distribution of the shear stress τ_{xy} along the shear-out region for the case of perfectly fitted pin and the two cases of interference fit. The stresses are normalized with the bearing reference stress σ_b=P/(d×t). A decrease in maximum shear

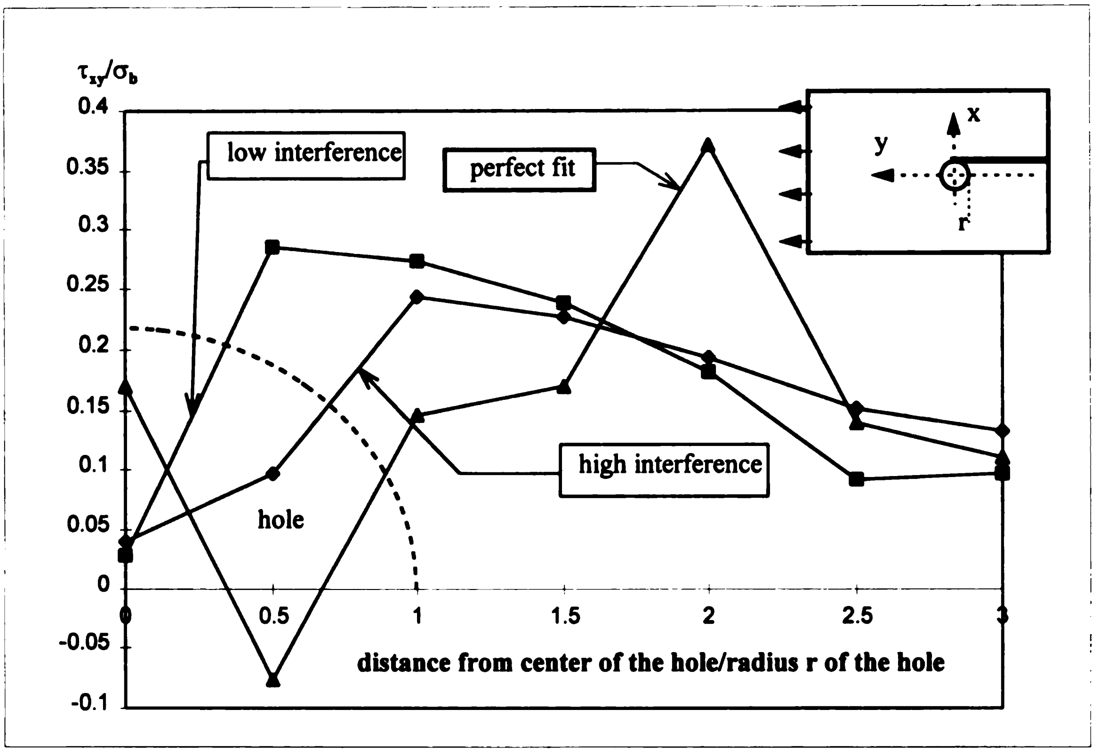

Figure 37. *Shear stress concentration factor τ_{xy}/σ_b along the shear-out region for (1) perfect fit, (2) low interference fit, (3) high interference fit.*

stress concentration factor is observed for the interference fits, this effect being larger for the high interference case. The maximum stress along the shear-out failure zone occurs at a distance from the horizontal diameter of the hole ("x" axis) equal to 2×r for the perfect fit case, 0.5×r for the low interference and 1×r for the high interference case.

As mentioned in Section 4.4 (Figure 31), the value of shear stress different from zero in the horizontal diameter on the edge of the hole ("x" axis) is due to friction effects (Zhang and Ueng 1984). In the case of perfect fit, relative slip between pin and hole can occur and this causes nonlinearities in load transfer mechanism from the pin to the plate, in the sense that doubling the load more than doubles the stress values near the hole (Lambert and Brailey 1962). This effect could contribute to the high value of shear stress at the horizontal diameter of the hole ("x" axis) in the case of perfect fit, as compared to the cases of interference fit, as shown in Figure 37.

Table 2 presents a summary of stress concentration factors (SCF's) obtained for the critical locations of ligament, bearing and shear-out regions, for the three cases of fit between pin and hole examined. It is worth noting that the ***absolute maximum*** stresses in the plots of Figures 35-37 are considered for the calculation of the SCF's in Table 2; these maximum values refer to different locations around the hole, as shown in Figures 35-37.

A decrease in all SCF's is observed going from perfect fit to low interference and to high interference fit.

Table 2. *Maximum stress concentration factors for ligament, bearing and shear-out regions for (1) perfect fit, (2) low interference fit and (3) high interference fit.*

STRESS CONCENTRATION FACTORS				
		perfect fit	"low" interference	"high" interference
ligament region	σ_{ymax}/σ_N	5.00	4.25	2.70
bearing region	σ_{ymax}/σ_b	0.4	0.25	0.18
shear-out region	τ_{xymax}/σ_b	0.37	0.29	0.24

CHAPTER VI

CONCLUSIONS AND RECOMMENDATIONS

An in-plane sensitive phase-stepped Digital Speckle Pattern Interferometer (DSPI) has been developed for high-precision strain/stress analysis. Parameters such as viewing camera aperture and lens magnification are adjusted in order to obtain maximum speckle contrast. The setup is calibrated using a rigidly-rotating plate. The DSPI correlation fringes obtained have sensitivity $\approx 0.67\mu m$/fringe and spatial resolution limit ≈ 1 fringe/mm of the object surface. The use of the phase-stepping technique and image filtering routines makes it possible to obtain a spatial resolution limit of the order of a few pixels and a very high sensitivity limit , which is virtually only subject to the limitation of the sampling of the images by the detector array of the viewing system. The maximum range of the measurable displacement, before speckle decorrelation occurred, is determined to be $\approx 17\mu m$.

The displacement maps are fitted with least-square polynomials, which are eventually differentiated along in-plane directions to obtain strains. The accuracy of this method for strain calculation is checked by comparing the results from DSPI with outputs from electrical resistance strain gages for the simple case of a cantilever beam, showing agreement to within 7%.

The technique has been applied to the study of single-pin joint in a glass-reinforced-epoxy laminate loaded through the pin. Strain and stress distributions near the hole are determined and stress concentration factors are calculated. A case of perfect ("push") fit and two cases of interference fit between pin and hole are investigated to study the effect of an interference fit on the stress distributions.

The major conclusions of this work are:

1) Digital Speckle Pattern Interferometry (DSPI) is a quick, simple and accurate method for experimental stress analysis. The use of a phase-stepping technique gives a spatial resolution limit of the order of a few pixels and a sensitivity limit only subject to the limitation of the sampling of the images by the imaging detector array.
2) A phase-stepping algorithm designed to be used in an out-of-plane sensitive setup can be also employed in an in-plane sensitive setup, if the system is properly calibrated.
3) The stress concentration near a pin loaded hole in a composite joint can be accurately determined through the use of phase-stepped DSPI.
4) Reduction in stress concentration factors up to a factor of 50% is observed when an interference fitted pin is used.

Although this study involves static loads, the results suggest that, in the case of varying pulsating load, the effect of interference is to decrease the oscillatory component of the stress at critical points near the hole and therefore increase the fatigue life of the component. The results found are limited to the case of elastic deformation of the specimen. Care must be used in choosing the right value of interference, because the combination of prestress and applied-load-induced stress can result in plastic yielding of the specimen. When this occurs, it is expected that fatigue strength is reduced (Jessop *et al.* 1956).

The measurement of the diameter of the hole is complicated by irregularities of the hole surface. The determination of the exact degree of interference between pin and hole used is probably affected by these errors.

The influence of an interference fit on the stress distribution of mechanically fastened joints needs more study, especially for the case of composite materials where several parameters such as fiber orientation, lay-up and mechanical properties contribute to complicate the stress field near the hole.

Possible future research areas are:

1) Investigation of reduction of stress concentration factors due to interference for different composite materials, lay-ups and/or fiber orientations.

2) Analytical and/or numerical studies to acquire a better understanding of the effect of interference on stress distribution near loaded holes.

3) Systematic investigation of different values of interference to find an optimum value which gives maximum stress concentration relief, for given material and geometry.

4) Studies on prediction of fatigue endurance of pin-loaded components under given loading conditions for different values of interference.

5) Development of a quick method for determination with high accuracy of the exact value of interference between pin and hole.

APPENDIX A

APPENDIX A

Displacement sensitivity in a dual-beam illumination DSPI setup with cylindrical illumination wavefronts

Let us suppose that a dual-beam illumination DSPI setup employs cylindrical illumination wavefronts, as shown in Figure A1.

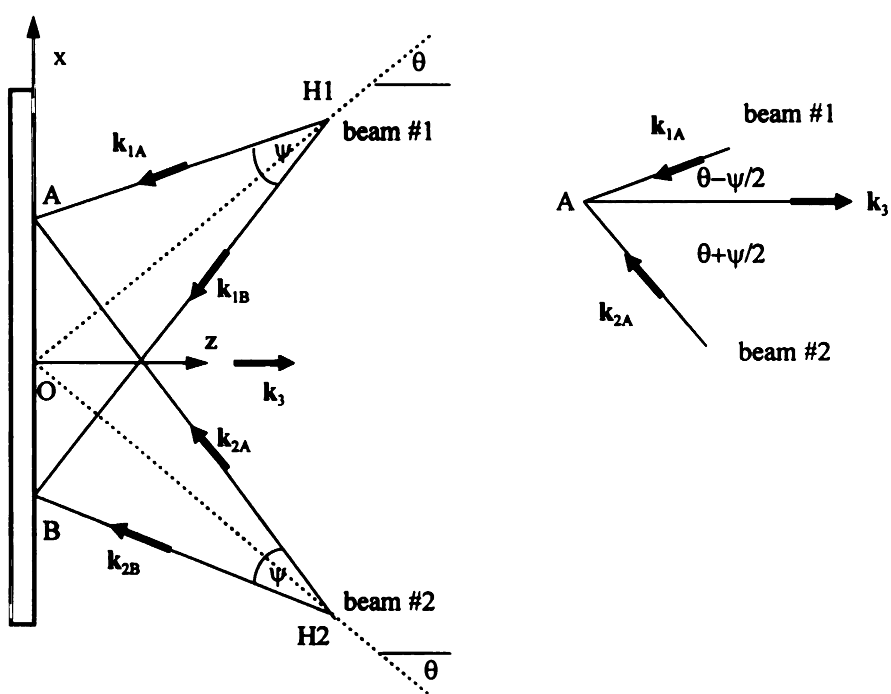

Figure A1. *Schematic of dual-beam illumination DSPI with cylindrical illumination wavefronts.*

The object lies in the (x,z) plane. The "z" direction is the viewing direction. The incidence angle of the illuminating beams changes across the x direction but is constant along the y direction coming out of the page ("cylindrical" wavefront). Suppose that this angle is θ at the center of the illuminated area (point "O" in Figure 38). Suppose also that the angle of illumination of each of the two beams (angle between unit vectors $\mathbf{k}_{1A}$ and $\mathbf{k}_{1B}$ and between $\mathbf{k}_{2A}$ and $\mathbf{k}_{2B}$ in Figure A1) is ψ.

Let us focus the attention on point A on the object and follow the same procedure used in Section 2.4.2 to calculate the sensitivity of this setup to the displacement components.

The total phase change in beam #1 at point A is:

$$\delta_1 = (\mathbf{k}_3 - \mathbf{k}_{1A}) \bullet \mathbf{d}$$

$$= \frac{2\pi}{\lambda}[\mathbf{k} - (-\sin(\theta - \frac{\psi}{2}) \cdot \mathbf{i} - \cos(\theta - \frac{\psi}{2}) \cdot \mathbf{k})] \cdot (d_x \cdot \mathbf{i} + d_y \cdot \mathbf{j} + d_z \cdot \mathbf{k})$$

$$= \frac{2\pi}{\lambda}[d_x \sin(\theta - \frac{\psi}{2}) + d_z(1 + \cos(\theta - \frac{\psi}{2})] \qquad \text{(A1)}$$

The total phase change in beam #2 at point A is:

$$\delta_2 = (\mathbf{k}_3 - \mathbf{k}_{2A}) \bullet \mathbf{d}$$

$$= \frac{2\pi}{\lambda}[\mathbf{k} - (\sin(\theta + \frac{\psi}{2}) \cdot \mathbf{i} - \cos(\theta + \frac{\psi}{2}) \cdot \mathbf{k})] \cdot (d_x \cdot \mathbf{i} + d_y \cdot \mathbf{j} + d_z \cdot \mathbf{k})$$

$$= \frac{2\pi}{\lambda}[-d_x \sin(\theta + \frac{\psi}{2}) + d_z(1 + \cos(\theta + \frac{\psi}{2})] \qquad \text{(A2)}$$

where: **i**, **j** and **k** are the unit vectors along the reference system (x,y,z);

$\mathbf{k}_3$, $\mathbf{k}_{1A}$, $\mathbf{k}_{2A}$, θ, ψ/2 are shown in Figure A1;

d is the displacement vector of point A on the object.

The phase change at point A due to the displacement **d** is the difference between δ_1 and δ_2, i.e.:

$$\Delta\phi_A = \frac{2\pi}{\lambda}[dx(2\sin\theta\cos\frac{\psi}{2}) + dz(2\sin\theta\sin\frac{\psi}{2})] \qquad \text{(A3)}$$

Equation (A3) shows that the phase change $\Delta\phi$ at point A is a function of *both* components of displacement d_x and d_z. The system is therefore sensitive not only to the in-plane component d_x but also to the out-of-plane component d_z.

For pure in-plane displacement (d_z=0), the sensitivity of the system is:

$$\frac{d_x}{n} = \frac{\lambda}{2\sin\theta\cos\frac{\psi}{2}} \qquad \text{(A4)}$$

where n is the fringe order.

For pure out-of-plane displacement (d_x=0), the sensitivity of the system is:

$$\frac{d_z}{n} = \frac{\lambda}{2\sin\theta\sin\frac{\psi}{2}} \qquad \text{(A5)}$$

By following the same procedure, the phase change at point B in Figure A1 results:

$$\Delta\phi_B = \frac{2\pi}{\lambda}[dx(2\sin\theta\cos\frac{\psi}{2}) - dz(2\sin\theta\sin\frac{\psi}{2})] \qquad \text{(A6)}$$

In a generic point P on the object different from A and B, the expression of the phase change $\Delta\phi$ is given by:

- equation (A3) for P laying between A and O in Figure A1;

- equation (A6) for P laying between O and B in Figure A1;

where the angle $\psi/2$ must be substituted with the actual illumination angle for point P (referring to Figure A1, angle between line H2-O and line H2-P or angle between line

H1-O and H1-P, being these two angles equal).

The sensitivity of the system to the displacement is therefore changing across the object surface. Figure A2 shows a computer-simulated measurement result for the dual-beam illumination DSPI setup using cylindrical illumination wavefronts with ψ=30° for a displacement field d_x=10μm, d_y=d_z=0.

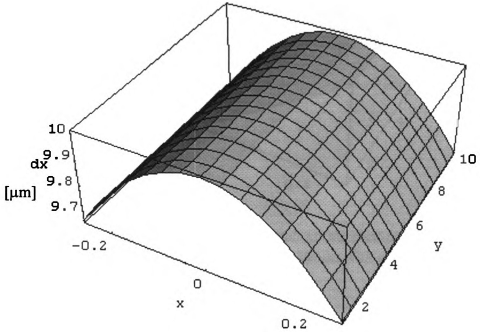

Figure A2. *Computer-simulated measurement result for the dual-beam illumination DSPI setup using cylindrical illumination wavefronts with ψ=30° for a displacement field d_x=10μm, d_y=d_z=0.*

A sensitivity compensation algorithm could be used to correct the measurement errors shown in Figure A2.

Figure A3 shows a computer-simulated measurement result for the dual-beam illumination DSPI setup using cylindrical illumination wavefronts with ψ=30° for a displacement field d_z=10μm, d_x=d_y=0.

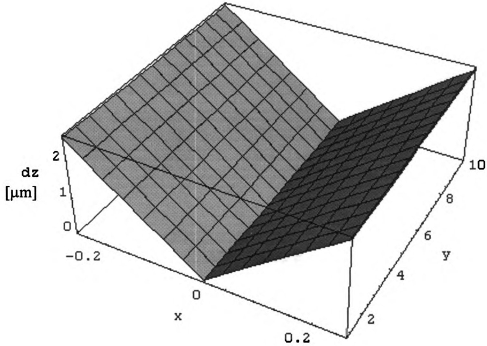

Figure A3. *Computer-simulated measurement result for the dual-beam illumination DSPI setup using cylindrical illumination wavefronts with ψ=30° for a displacement field d_z=10μm, d_x=d_y=0.*

If the illuminating beams have plane wave fronts, ψ=0, and equations (A3) and (A6) coincide with equation (12) in Section 2.4.2, which is the case of the setup sensitive *only* to the in-plane component d_x of displacement.

APPENDIX B

APPENDIX B

Displacement field in rigid in-plane rotation of a plate

Let us suppose that a rectangular plate is rotated rigidly by an angle θ in the plane (x,y), as shown in Figure B1. Let us also assume that θ is small, so that the displacement vector at any point on the plate can be considered tangent to the trajectory of the point.

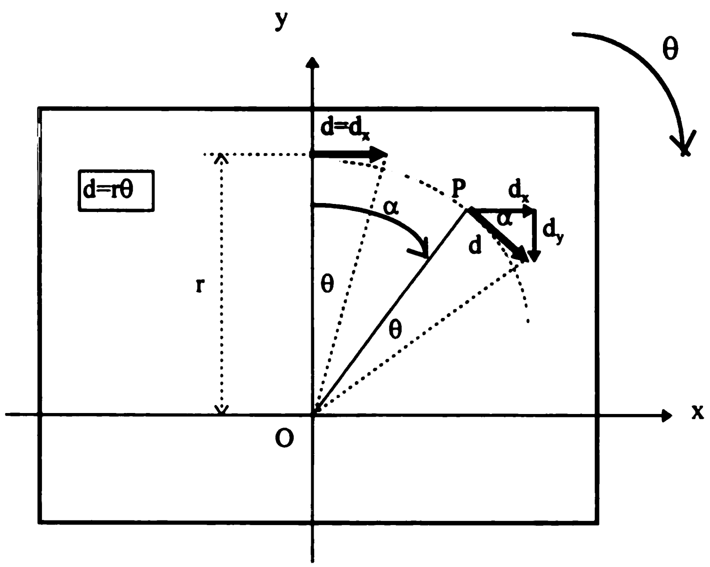

Figure B1. *Displacement field in an in-plane rotation of a plate, for a small angle of rotation θ.*

For a generic point P distant r from the center of rotation O and whose position vector forms an angle α with the "y" axis, the two in-plane components of the displacement are:

$d_x = d^* \cos\alpha = r\theta\cos\alpha$ (B1)

$d_y = d^* \sin\alpha = r\theta\sin\alpha$ (B2)

Figures B2 and B3 show respectively the d_x and the d_y component of the displacement for a 10×10 mm^2 plate rotated by an angle θ=5°. Note that the d_x component is linear along the "y" direction and constant along the "x" direction. The opposite is true for the d_y component.

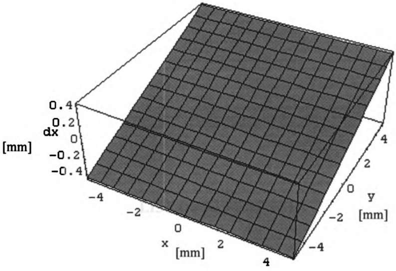

Figure B2.*dx component for a 10×10 mm^2 plate rotated by an angle θ=5°.*

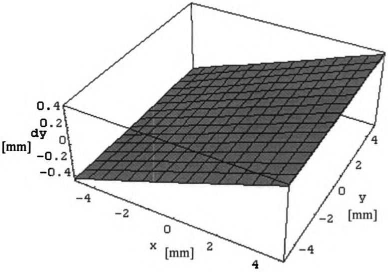

Figure B3. *dy component for a 10×10 mm^2 plate rotated by an angle θ=5°.*

LIST OF REFERENCES

LIST OF REFERENCES

Carre', P. (1966). "Installation et utilisation du comparateur photoelectrique et interferentiel du Bureau International des Poids et Mesures." Metrologia, 2, 1: 13-23.

Chang, F.K., Scott, R.A., and Springer G.S. (1984). "Design of composite laminates containing pin loaded holes." Journal of Composite Materials, 18, 3: 279-289.

Chang, M., Hu, C.P., Lam, P., and Wyant, C. (1985). "High precision deformation measurement by digital phase shifting holographic interferometry." Applied Optics, 24, 22: 3780-3783.

Chawla, K.K. (1987). Composite Materials. New York: Springer-Verlag.

Chen, X. (1995). Electronic Speckle Pattern Interferometry, Electronic Shereography and their applications. Ph.D. Dissertation, Michigan State University.

Cloud, G.L. (1975). "Practical Speckle Interferometry for measuring in-plane deformations." Applied Optics, 14, 4: 878-884.

Cloud, G.L. (1995). Optical methods of engineering analysis: Cambridge University Press.

Cloud, G.L., and Nokes, J.P. (1993). "The application of interferometric techniques to the NDE of composite materials." Proceedings of SEM Spring Conference on Experimental Mechanics, Dearborn, Michigan: 358-365.

Cloud, G.L., Sikarskie, D., Vable, M., Herrera Franco, P., and Bayer, M. (1987). "Experimental and theoretical investigation of mechanically fastened composites." Tech. Rep. TACOM-TR-12844, U.S. Army Tank-Automotive Command Research, Development and Engineering Center, Warren, Michigan 48397-5000.

Cohen, D., Hyer, M.W., Shuart, M.J., Griffin, O.H., Prasad, C., and Yamalachili, S.R. (1995). "Failure criterion for thick multifastener graphite-epoxy composite joints." Journal of Composites Technology & Research, JCTRER, 17, 3: 237-248.

Cole, R.T., Bateh, E.J., and Potter, J. (1982). "Fasteners for composite structures." Composites, 13, 3: 233-240.

Collings, T.A. (1977). "The strength of bolted joints in multi-directional cfrp laminates." Composites, 8, 1: 43-55.

Collings, T.A. (1982). "On the bearing strengths of CFRP laminates." Composites, 13, 3: 241-252.

Creath, K. (1984). "Digital Speckle Pattern Interferometry (DSPI) using a 100×100 imaging array." SPIE, 501: 292-298.

Creath, K. (1985). "Phase-shifting speckle interferometry." Applied Optics, 24, 18: 3053-3058.

Creath, K. (1988). "Phase measurement interferometry methods." In Progress in Optics, 26: 349-393. Amsterdam: Elsevier Science Publishers.

Creath, K., Cheng, Y.Y., and Wyant, J.C. (1985). "Conturing aspheric surfaces using two-wavelength phase-shifting interferometry." Optica Acta, 32, 12:1455-1464.

Czarnek, R., Post, D., and Guo, Y.(1987). "Strain concentration factors in composite tensile members with central holes." Proceedings of SEM Spring Conference on Experimental Mechanics, Houston, Texas: 657-663.

De Jong, T. (1977). "Stresses around pin-loaded holes in elastically orthotropic or isotropic plates." Journal of Composite Materials, July 1977, 11: 313-331.

Eriksson, L.I. (1986). "Contact stresses in bolted joints of composite laminates." Composite Structures, 6, 1-3: 57-75.

Floureux, T. (1993). "Improvement of electronic speckle fringes by addition of incremental images." Optics&Laser Technology, 25, 4: 255-258.

Ford, S.C., Leis, B.N., Utah, D.A., Griffith, W., Sampath, S.G., and Mincer, P.N. (1975). "Interference-fit fastener investigation." Tech. Rep. AFFDL-TR-75-93, Air Force Dynamics Laboratory, WPAFB, Ohio 45433.

Frocht, M.M., and Hill, H.N. (1940). "Stress-concentration factors around a central circular hole in a plate loaded through pin in the hole." Journal of Applied Mechanics, 7, 1: 5-9.

Godwin, E.W., and Matthews, F.L. (1980). "A review of the strength of joints in fiber-reinforced plastics. Part 1-Mechanically fastened joints." Composites, 11, 3: 155-160.

Greivenkamp, C.J. (1984). "Generalized data reduction for heterodyne interferometry." Optical Engineering, 23, 4: 350-352.

Gulker, G., Hinsch, K., Holscher, C., Kramer, A., and Neunaber, H. (1990). "Electronic speckle pattern interferometry system for in situ deformation monitoring on buildings." Optical Engineering, 29, 7: 816-820.

Herrera Franco, P. (1985). A study of mechanically fastened composite using high sensitivity interferometric Moire technique. Ph.D. Dissertation, Michigan State University.

Hornbeck, R.W. (1975). Numerical Methods. Englewood Cliffs, New Jersey: Prentice-Hall Inc.

Hyer, M.W., Klang, E.C., and Cooper, D.E. (1987). "The effects of pin elasticity, clearance and friction on the stresses in a pin-loaded orthotropic plate." Journal of Composite Materials, 21, 3: 190-206.

Jessop, H.T., Snell, C., and Holister, G.S. (1956). "Photoelastic investigation on plates with single interference-fit pins with load applied to plate only." The Aeronautical Quarterly, November 1956, 7: 297-314.

Jessop, H.T., Snell, C., and Holister, G.S. (1958). "Photoelastic investigation on plates with single interference-fit pins with load applied (a) to pin only and (b) to pin and plate simultaneously." The Aeronautical Quarterly, May 1958, 9: 147-163.

Jia, Z., and Shah, S.P. (1994). "Two-dimensional electronic-speckle-pattern interferometry and concrete-fracture processes." Experimental Mechanics, 34, 3:
262-270.

Jin, G., and Tang, S. (1992). "Electronic speckle pattern interferometry with a polarization phase-shift technique." Optical Engineering, 31, 4: 857-860.

Joenathan, C. (1991). "Recent Developments in Electronic Speckle Pattern Interferometry." Proceedings of SEM Spring Conference on Experimental Mechanics, Milwaukee, Wisconsin: 198-204.

Joenathan, C., and Khorana, B.M. (1992). "Contrast of the vibration fringes in time-averaged electronic speckle-pattern interferometry: effect of speckle averaging." Applied Optics, 31, 11: 1863-1870.

Joenathan, C., and Khorana, B.M. (1992). "Phase-measuring fiber optic electronic speckle pattern interferometer: phase step calibration and phase drift minimization." Optical Engineering, 31, 2: 315-321.

Joenathan, C., Pfister, B., and Tiziani, H.J. (1990). "Contouring by electronic speckle pattern interferometry employing dual beam illumination." Applied Optics, 29, 13: 1905-1911.

Jones, R., and Wykes, C. (1983). Holographic and Speckle Interferometry, 1st edition: Cambridge University Press.

Lambert, T.H., and Brailey, R.J. (1962). "The influence of the coefficient of friction on the elastic stress concentration factor for a pin-jointed connection." The Aeronautical Quarterly, February 1962, 13: 17-29.

Leendertz, J.A. (1970). "Interferometric displacement measurement on scattering surfaces utilizing speckle effect." Journal of Physics E: Scientific Instruments, 3: 214-218.

Lekhnitskii, S.G., Tsai, S.W., and Cheron, T. (1968). Anisotropic Plates. New York, London and Paris: Gordon and Breach Science Publishers.

Love, T.S. (1963). "Study of stress patterns around prestressed holes subject to various loading parameters." General Dynamics Fort Worth Division Report ERR-FW-436.

Matthews, F.L. (1987). Joining fiber-reinforced plastics. London and New York: Elsevier Applied Science.

Matthews, F.L., Wong, C.M., and Chryssafitis, S. (1982). "Stress distribution around a single bolt in fibre-reinforced plastic." Composites, 13, 3: 316-322.

Mendoza Santoyo, F., Shellabear, M.C., and Tyrer, J.R. (1991). "Whole field in-plane vibration analysis using pulsed phase-stepped ESPI." Applied Optics, 30, 7: 717-721.

Morimoto, Y., and Fujisawa, M. (1993). "Fringe pattern analysis by extraction of characteristics using image processing." Proceedings of SEM Spring Conference on Experimental Mechanics, Dearborn, Michigan: 36-44.

Morimoto, Y., and Fujisawa, M. (1994). "Fringe pattern analysis by a phase-shifting method using Fourier transform." Optical Engineering, 33, 11: 3709-3714.

Nisida, M., and Saito, H. (1966). "Stress distribution in a semi-infinite plate due to a pin determined by interferometric method." Experimental Mechanics, 6, 5: 273-279.

Perry, K.E.jr., and McKelvie, J. (1993). "An investigation of delamination in composite materials using phase shifting Moire Interferometry." Proceedings of SEM Spring Conference on Experimental Mechanics, Dearborn, Michigan: 298-306.

Pradhan, B., and Ray, K. (1984). "Stresses around partial contact pin-loaded holes in FRP composite plates." Journal of Reinforced Plastics and Composites, 3, 1: 69-84.

Preater, R.W.T. (1984). "Analysis of rotating component strains using electronic speckle pattern interferometry." SPIE, Symposium OPTIKA, Budapest, Hungary, 473: 40-43.

Ramamurthy, T.S. (1989). "Recent studies on the behavior of interference fit pins in composite plates." Composite Structures, 13, 2: 81-99.

Ramamurthy, T.S. (1990). "Analysis of interference fit pin joints subjected to bearing bypass load." AIAA Journal, 28, 10: 1800-1805.

Ratnam, M.M., Evans, W.T., and Tyrer, J.R. (1992). "Measurement of thermal expansion of a piston using holographic and electronic speckle pattern interferometry." Optical

Engineering, 31, 1: 61-69.

Regalbuto, J.A., and Wheeler, O.E. (1970). "Stress distributions from interference fits and uniaxial tension." Experimental Mechanics, 10, 7: 274-280.

Rowland, R.E., Rahman, M.U., Wilkinson, T.L., and Chiang, Y.I. (1982). "Single- and multiple-bolted joints in orthotropic materials." Composites, 13, 3: 273-279.

Sendeckyj, G.P., and Richardson, M.D. (1974). "Fatigue behavior of a graphite-epoxy laminate loaded through an interference-fit pin." Proceedings of 2nd Air Force Conference on Fibrous Composites in Flight Vehicle Design, Tech. Rep. AFFDL-TR-74-103, Air Force Flight Dynamics Lab, WPAFB, Ohio.

Shames, I.H. (1964). Mechanics of Deformable Solids. Englewood Cliffs, New Jersey: Prentice-Hall Inc.

Theocratis, P.S. (1956). "The stress distribution in a strip loaded in tension by means of a central pin." Journal of Applied Mechanics, 23, 1: 85-90.

Van Wingerden, J., Frankena, H.J., and Smorenburg, C. (1991). "Linear approximation for measurement errors in phase shifting interferometry." Applied Optics, 30, 19: 2718-2729.

Vest, C.M. (1979). Holographic Interferometry, New York: John Wiley and Sons.

Vikhagen, E. (1991). "TV Holography: spatial resolution and signal resolution in deformation analysis." Applied Optics, 30, 4: 420-425.

Vikhagen, E., and Malmo, J.T. (1991). "Phase shifting TV-holography: theory and applications." Proceedings of SEM Spring Conference on Experimental Mechanics, Milwaukee, Wisconsin: 163-165.

Vrooman, H.A. and Maas, A.M. (1991). "Image processing algorithms for the analysis of phase-shifted speckle interference patterns." Applied Optics, 30, 13: 1636-1641.

Whitney, J.M., Daniel, I.M., and Pipes, R.B. (1982). Experimental Mechanics of fiber reinforced composite materials, 1st edition Monograph No.4 Brookfield Center, Connecticut: Society for Experimental Stress Analysis.

Winther, S., and Slettemoen, G.A. (1984). "An ESPI contouring technique in strain analysis." SPIE, Symposium OPTIKA, Budapest, Hungary, 473: 44-47.

Wong, C.M.S., and Matthews, F.L. (1981). "A finite element analysis of single and two-hole bolted joints in fiber reinforced plastic." Journal of Composite Materials, September 1981, 15: 481-491.

Zhang, K.D., and Ueng, C.E.S. (1984). "Stresses around a pin-loaded hole in orthotropic plates." Journal of Composite Materials, 18, 5: 432-446.

Zou, Y., Diao, H., Peng, X., and Tiziani, H. (1992). "Contouring by electronic speckle pattern interferometry with quadruple-beam illumination." Applied Optics, 31, 31: 6599-6602.

Zou, Y., Diao, H., Peng, X., and Tiziani, H. (1992). "Geometry for contouring by electronic speckle pattern interferometry based on shifting illumination beams." Applied Optics, 31, 31: 6616-6621.